Heat transfer enhancement compared to entropy generation by imposing magnetic field and hybrid nanoparticles in mixed convection of a Bingham plastic fluid in a ventilated enclosure

Received 14 September 2021
Revised 8 December 2021
Accepted 12 December 2021

Subhasree Dutta and Somnath Bhattacharyya
Department of Mathematics, Indian Institute of Technology Kharagpur, Kharagpur, India, and

Ioan Pop
Facultatea de Matematica si Informatica, Universitatea Babes Bolyai, Cluj-Napoca, Romania

Abstract

Purpose – The purpose of this study is to analyze the nonhomogeneous model on the mixed convection of Al2O3–Fe3O4 Bingham plastic hybrid nanofluid in a ventilated enclosure subject to an externally imposed uniform magnetic field. Entropy generation and the pressure drop are determined to analyze the performance of the heat transfer. The significance of Joule heating arising due to the applied magnetic field on the heat transfer of the yield stress fluid is described.

Design/methodology/approach – The ventilation in the enclosure of heated walls is created by an opening on one vertical wall through which cold fluid is injected and another opening on the opposite vertical wall through which fluid can flow out.

Findings – This study finds that the inclusion of Fe_3O_4 nanoparticles with the Al_2O_3-viscoplastic nanofluid augments the heat transfer. This rate of enhancement in heat transfer is higher than the rate by which the entropy generation is increased as well as the enhancement in the pressure drop. The yield stress has an adverse effect on the heat transfer; however, it favors thermal mixing. The magnetic field, which is acting opposite to the direction of the inlet jet, manifests heat transfer of the viscoplastic hybrid nanofluid. The horizontal jet of cold fluid produces the optimal heat transfer.

Originality/value – The objective of this study is to analyze the impact of the inclined cold jet of viscoplastic electrically conducting hybrid nanofluid on heat transfer from the enclosure in the presence of a uniform magnetic field. The combined effect of hybrid nanoparticles and a magnetic field to enhance heat transfer of a viscoplastic fluid in a ventilated enclosure has not been addressed before.

Keywords Entropy generation, MHD, Mixed convection, Nonhomogeneous model, Ventilated enclosure, Viscoplastic hybrid nanofluid

Paper type Research paper

Nomenclature

Bn = Bingham number, $\tau_0^* H/\eta U_0$;
c_p = Specific heat (J kg^{-1} K^{-1});
D_B = Brownian diffusion coefficient, $K_B T/3\pi\mu_f d_p$;

International Journal of Numerical Methods for Heat & Fluid Flow
Vol. 32 No. 9, 2022
pp. 3007-3038

0961-5539
DOI 10.1108/HFF-09-2021-0623

D_T = Thermophoretic diffusion coefficient, $0.26(K_f\mu_f\varphi_b)/(K_p + 2K_f)\rho_f$;
g = Gravitational acceleration (m/s^2);
Gr = Grashof number, $(1 - \varphi_b)\left(\beta_f g\Delta T H^3\right)/\nu_f{}^2$;
H = Enclosure height, (m);
Ha = Hartmann number, $B_0 H\sqrt{\sigma_f/\mu_f}$;
J = Joule heating parameter, $H\sigma_f B_0^2 u_0/\left(\rho C_p\right)_f (T_h - T_c)$;
k = Thermal conductivity (W/m K);
Nr = Buoyancy ratio, $\varphi_b(\rho_{p_i} - \rho_f)/\{\rho_f\beta_f\Delta T(1 - \varphi_b)\}$;
Nu = Local Nusselt number, $\{-(knf/kf)\,(\partial\theta/\partial n)\}$;
p^* = Pressure, (N/m^2);
Pr = Prandtl number, ν_f/α_f;
Re = Reynolds number, $\rho_f U_0 H/\mu_f$;
Ri = Richardson number, Gr/Re^2;
S_{gen} = Dimensionless total entropy generation;
S_{av} = Average entropy generation;
t^* = Time (s);
t = Dimensionless time;
T = Temperature (K);
(u^*, v^*) = Velocity components in x- and y-direction, respectively (m/s);
(u, v) = Dimensionless velocity components in x- and y-direction, respectively; and
U_0 = Characteristic velocity of the flow (m/s).

Greek symbols

α = Thermal diffusivity (m^2/s);
β = Coefficient of thermal expansion;
λ = Inclination angle of jet flow;
μ = Dynamic viscosity (kg/m s);
ν = Kinematic viscosity (m^2/s);
θ = Dimensionless temperature;
ρ = Density, (kg/m^3); and
φ = Nanoparticles volume fraction.

Subscripts

av = Average value;
b = Bulk value;
f = Clear fluid;
nf = Hybrid nanofluid;
p = Solid particle; and
$i = 1, 2$ = Al_2O_3/Fe_3O_4 nanoparticles.

Superscripts

$*$ = Dimensional quantity; and
0 = Clear fluid ($\varphi_b = 0$).

1. Introduction

Ventilated enclosures having an inlet and outlet port is one of those configurations where both the shear dominated forced convection and buoyancy driven natural convection occur

simultaneously. Ventilation is a useful mechanism to maintain thermal balance between heating and cooling by minimizing the energy consumption (Bianco *et al.*, 2018; Koufi *et al.*, 2017). Thermal management in ventilated enclosures provides a guideline for designing computer chips, heat exchangers, refrigerator, cooling of electronic devices, room heating and solar panel (Gupta *et al.*, 2015). Several authors (Arroub *et al.*, 2016; Bilgen and Muftuoglu, 2008) studied the mixed convection within a ventilated enclosure by considering different thermal boundary conditions to achieve an enhanced thermal performance. The experimental and numerical studies (Ingole and Sundaram, 2016; Shiriny *et al.*, 2019) show that the direction of the injection flow at the inlet has dependency on the thermal performance of the enclosure.

The impact of nanofluid on heat transfer and pressure drop in a ventilated cavity is analyzed by several authors (Kherroubi *et al.*, 2020; Sourtiji *et al.*, 2014, 2011). These studies show that the rate of heat transfer intensifies due to the inclusion of nanoparticles in the base fluid. Sourtiji *et al.* (2014) conclude that maximum heat transfer is achieved by placing the outlet port at the end corner, whereas the minimum heat transfer is achieved when the outlet port is fixed at the middle of the side wall. Recently, Kherroubi *et al.* (2020) investigated the impact of the nanofluid on the three-dimensional fluid flow and heat transfer by considering a ventilated cubic enclosure having heated side walls and concluded that the use of nanoparticles improves the thermal performance of the fluid but increases the pressure drop coefficient significantly. All those studies on heat transfer in a ventilated enclosure deals with Newtonian fluid with a single type of nanoparticle suspended in it.

In recent years, a superior category of nanofluids, the "hybrid nanofluid" composed of more than one type of nanoparticles mixed with the base liquid, has been established to provide better thermal characteristics such as higher thermal conductivity, chemical stability and mechanical resistance as compared with the individual nanofluids (Esfe *et al.*, 2015; Ghalambaz *et al.*, 2020b). This extended type of nanofluid is widely used in several heat transfer fields such as motor cooling, thermal management of vehicles, transformer cooling and refrigeration due to its improved efficiency over that of the single type nanofluids (Ellahi *et al.*, 2019; Ghalambaz *et al.*, 2020a; Khan *et al.*, 2020b). Heat transfer augmentation in magnetohydrodynamics (MHD) forced convection within an enclosure by considering the Ag–MgO–water hybrid nanofluid is studied numerically by Ma *et al.* (2019). Indeed, contradictory results also exist in the literature. The agglomeration of different types of nanoparticles may cause a reduction in the thermal conductivity of the hybrid nanofluid (Sarkar *et al.*, 2015). Mehryan *et al.* (2019) analyzed the impact of using Cu and Al_2O_3 nanoparticles for the hybridization and concluded that for a low Rayleigh number, hybrid nanofluid produces a higher heat transfer rate. However, for a higher range of the Rayleigh number, the hybrid nanoparticles reduce the heat transfer compared with the Al_2O_3-nanofluid due to the increased dynamic viscosity of the hybrid nanofluid. Studies on hybrid nanofluids are important to achieve enhanced thermal performance by using expensive nanoparticles with minimum quantity (Rashad *et al.*, 2018). For example, the price of copper nanoparticles is about 10 times greater than that of alumina nanoparticles.

The hydrodynamics of nanofluid can be analyzed based on the homogeneous model in which the nanoparticles are considered to move with the fluid, and uniform distribution of nanoparticles in the fluid is assumed (Dogonchi *et al.*, 2019a). In the nonhomogeneous model of the nanofluid, a relative flux between the fluid and nanoparticles is accounted for, which develops a nonhomogeneous distribution of the nanoparticles in the medium. Buongiorno (2006) demonstrated the nonhomogeneous model by considering that the slip velocity between nanoparticles and fluid can be generated by seven mechanisms, namely, Brownian

diffusion, thermophoresis, diffusiophoresis, inertia, Magnus effect, fluid drainage and gravity, of which only the Brownian and thermophoretic diffusion have a significant contribution. In the absence of a turbulent effect, the thermophoretic force influence to migration of the nanoparticles in the opposite direction of the imposed temperature gradient, whereas Brownian diffusion increases the homogeneity in the nanoparticles distribution due to the higher concentration gradient of the nanoparticles. It has been established by several authors (Corcione, 2010; Ho *et al.*, 2010) that the nonhomogeneous model has better agreement with the experimental data. The comparative study (Esfandiary *et al.*, 2016) between the homogeneous and the nonhomogeneous model shows that Brownian diffusion and thermophoresis have a significant impact on the heat transfer performance of the nanofluid. The nonhomogeneous model provides a higher heat transfer rate than the homogeneous model due to the presence of slip velocity between the fluids and nanoparticles. Although the contradictory result is also being reported in the literature (Sheikhzadeh *et al.*, 2013) i.e. the single-phase homogeneous model generates a higher heat transfer rate in comparison with the two-phase nonhomogeneous model. Garoosi *et al.* (2014) have shown that instead of a monotonic increment of average Nusselt number with the nanoparticles volume fraction as is seen in the homogeneous model, the nonhomogeneous model shows that there exists an optimal volume fraction at which the maximum heat transfer occurs.

Most of the studies on convective heat transfer are confined to the Newtonian fluid, where the dynamic viscosity of the fluid is constant throughout the flow domain. In the case of the nonNewtonian fluid, the viscosity is not constant; rather, it depends on the rate of the strain, which is governed by a constitutive equation of the strain tensor (Nazari *et al.*, 2020). A class of nonNewtonian fluid, the viscoplastic fluid, which involves a suspension of macromolecules, can model effectively the hydrodynamics of blood, synovial fluids, saliva, bitumen, honey, paste, animal waste slurries, cement paste, greases, molten lava, magmas, paints, pharmaceutical products and wet beach sand (Elelamy *et al.*, 2020; Kefayati and Tang, 2018). The growing applications of the viscoplastic fluid in various manufacturing and processing industries (Syrakos *et al.*, 2013) have primed us to analyze the flow and heat transfer characteristics of such types of nonNewtonian fluid. The viscoplastic fluid possesses the characteristic that it flows when the shear stress exceeds a critical value τ_0, the yield stress. For shear stress below the yield stress, the viscoplastic fluid either remains stationary or moves like a rigid body. The Bingham viscoplastic fluid involves unyielded zones with a discontinuity in shear stress across the yield surface. To avoid such discontinuity along the yield surface, Papanastasiou (1987) proposed a regularization approach by introducing the stress growth parameter through which the constitutive equation is made to be valid throughout the flow domain without involving any discontinuity across the yield surface. This regularization approach is adopted by several authors to analyze the flow behavior of the viscoplastic fluid (Kefayati, 2017, 2018; Kefayati and Huilgol, 2016).

Studies based on the homogeneous model for the mixed convection of the Bingham plastic nanofluid inside a square enclosure is made by Kefayati and Huilgol (2016) and Kefayati (2018). In those studies, the regularization approach was adopted to analyze the mixed convection of the yield stress viscoplastic fluid. Studies on nonNewtonian nanofluids based on the two-phase model are limited to power-law fluids only. Kefayati (2017) considered the nonhomogeneous model to study the mixed convection of the shear-thinning nonNewtonian nanofluid based on the power-law model and found that the Brownian diffusion and thermophoresis decline the rate of heat transfer. Our literature survey

suggests that a detailed study on the heat transfer of viscoplastic nanofluid based on the nonhomogeneous model has not been made.

Several studies established that a transverse magnetic field imposed opposite to the direction of the primary flow can produce a higher heat transfer in a channel or enclosure (Heidary *et al.*, 2015). The magnetic field-induced Lorentz force creates a strong influence on the thermal field by diminishing the recirculating vortices in the enclosure and modifying the boundary layers along the side walls (Dogonchi *et al.*, 2019b; Tayebi and Chamkha, 2019). Recently, Kefayati and Tang (2018) studied the MHD mixed convection in a lid-driven cavity and found that the adverse Lorentz force due to the imposed magnetic field expands the unyielded regions leading to a reduction in heat transfer. The impact of a uniform magnetic field on the heat transfer of nanofluids in a cavity or channel is considered by several researchers (Khan *et al.*, 2020a; Rashad *et al.*, 2018; Rasool *et al.*, 2020). The Joule heating arises due to the imposed magnetic field on the electrically conducting fluid enhancing the fluid temperature; however, it may have a marginal effect on the formation of unyielded zones of the viscoplastic fluid. The convective heat transfer of Al_2O_3–water nanofluid considering the magnetic field together with Joule heating effect is analyzed by Mehmood *et al.* (2017) and concluded that the Joule heating creates an adverse effect on the heat transfer.

In this paper, we have considered mixed convection of a viscoplastic nanofluid subjected to an applied magnetic field. The MHD convection of viscoplastic fluid has relevance in the context of several physiological applications such as heart valve prosthesis, cell separation and magnetic hyperthermia. The human blood can be considered to be electrically conducting nonNewtonian fluid (Majee and Shit, 2017). The magnetic field is also used to regulate the blood flow during surgery as the flow rate is enhanced due to the magnetic properties of blood (Haik *et al.*, 2001). Heat transfer analysis in an enclosure filled with viscoplastic fluid, influenced by an externally imposed magnetic field, has relevance in polymer industry, plasma studies, electronic package, geothermal energy extraction, MHD generators, microelectromechanical systems and many other areas of engineering (Sheremet *et al.*, 2016).

The entropy generation, which is determined based on the second law of thermodynamics, provides a measure of the thermodynamic efficiency of the system (Bejan, 1980). The relative influence of the irreversibilities generated due to thermal radiation and viscous dissipation is illustrated by computing the Bejan number (Varol *et al.*, 2008). Several researchers (Bejan, 1980; Ellahi *et al.*, 2018) assessed the thermal efficiency of a system by evaluating the entropy generation. Using the homogeneous model for nanofluid, the heat transfer efficiency of the viscoplastic nanofluid based on the entropy generation is made by several authors (Kefayati, 2018; Mohammadi and Moghadam, 2015). However, the entropy generation to evaluate the thermal performance of the viscoplastic fluid in a ventilated enclosure has not been addressed in the literature.

We have studied the mixed convection of the Bingham plastic hybrid nanofluid in a ventilated enclosure that is subjected to a uniform horizontal magnetic field. An inclined jet of cold $Al_2O_3-Fe_3O_4$/viscoplastic hybrid nanofluid is pumped through the inlet of the enclosure of heated side walls, and an outlet port is fixed at the lower corner of the opposite side wall. A uniform magnetic field is applied opposite to the direction of the inward jet. The buoyancy force, generated by the temperature gradient due to the four heated side walls together with the shear force governed by the incoming flow from the inlet, creates the mixed convection within the enclosure. The objectives of the present study are to augment the heat transfer of the viscoplastic fluid in mixed convection through the inclusion of $Al_2O_3-Fe_3O_4$ hybrid nanoparticles and imposed magnetic field, as well as to investigate the

thermal performance of the hybrid nanofluid compared with a nanofluid composed of a single type of nanoparticles. The nonhomogeneous model is adopted to study the mixed convection of the hybrid viscoplastic plastic nanofluid. The heat transfer augmentation of a viscoplastic fluid in a ventilated enclosure through the combined effect of the hybrid nanoparticles and magnetic field has not been addressed before. In addition, none of the existing studies on viscoplastic nanofluid in a ventilated enclosure evaluated the entropy generation to describe the heat transfer performance.

We have adopted the regularization method (Papanastasiou, 1987) to model the viscoplastic fluid. The present model for the nonNewtonian fluid flow is validated by comparing it with the existing experimental results of Hassan *et al.* (2020). Entropy generation along with the Bejan number, thermal mixing and pressure drop between the inlet and outlet are determined to evaluate the heat transfer performance of the vented enclosure. The irreversibility due to the imposed magnetic field is included in the entropy generation. The yield stress of the viscoplastic fluid attenuates heat transfer, which can be compensated by the magnetic field applied in the reverse direction of the incoming jet. We find that for nonzero yield stress, the results based on the present nonhomogeneous model differ significantly from the corresponding results due to the homogeneous models. Based on this study, we have established that improved thermal performance can be achieved by considering the hybrid nanofluid compared with a nanofluid composed of a single type of nanoparticles.

2. Mathematical model

We consider the laminar two-dimensional mixed convection of an electrically conducting hybrid nanofluid, modeled as Bingham plastic fluid, inside a ventilated enclosure of height H having the inlet and outlet ports at the top of the left and the bottom of the right vertical walls, respectively [Figure 1(a)]. All four walls of the enclosure are maintained at higher temperature T_h, whereas the fluid flowing in through the inlet port is considered to be at a lower temperature T_c ($< T_h$). The inlet fluid velocity U_0 is considered to be injected at an angle λ with the horizontal (x-axis). A magnetic field of uniform strength B_0 is applied horizontally opposite to the direction of the jet flow. The hybrid nanofluid, composed of the

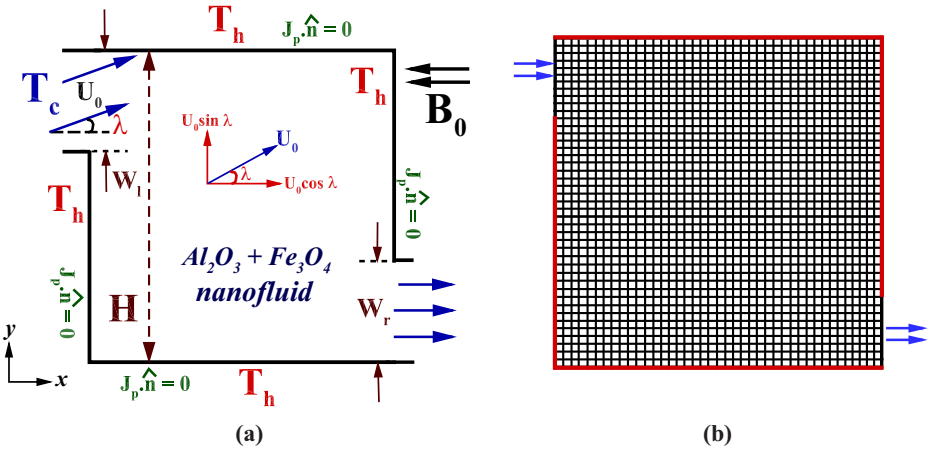

Figure 1.
(a) Schematic diagram of the physical domain with boundary conditions; (b) uniform mesh distribution in the computational domain

dilute mixture of solid spherical nanoparticles Al_2O_3 and Fe_3O_4 to the electrically conducting base fluid, is considered to exhibit a viscoplastic nature. The induced magnetic field generated due to the motion of the nanofluid is assumed to be negligible compared with the applied magnetic field. The impact of Joule heating generated due to the imposed magnetic field in the energy transport equations is considered in our study. The width of the inlet and outlet port are the same, i.e. $W_r = W_l = H/3$.

The constitutive equation for the Bingham plastic fluid relates the shear stress (τ*) with the shear strain rate ($\dot{\gamma}^*$) (Kefayati, 2018) i.e.

$$\begin{cases} \tau^* = \left(\eta + \dfrac{{\tau_0}^*}{|\dot{\gamma}^*|}\right)\dot{\gamma}^*, & \text{for } |\tau^*| > {\tau_0}^* \\ \gamma^* = 0, & \text{for } |\tau^*| \le {\tau_0}^* \end{cases} \tag{1}$$

where ${\tau_0}^*$ is the yield stress of the viscoplastic fluid, and the constant η is the flow consistency index. The shear strain rate is $|\dot{\gamma}^*| = \left[2\left(\frac{\partial u^*}{\partial x}\right)^2 + 2\left(\frac{\partial v^*}{\partial y}\right)^2 + \left(\frac{\partial u^*}{\partial y} + \frac{\partial v^*}{\partial x}\right)^2\right]^{\frac{1}{2}}$. It is apparent that in the viscoplastic fluid flow, two distinct domains, namely, yielded region ($|\tau^*| > {\tau_0}^*$) and unyielded region ($|\tau^*| \le {\tau_0}^*$) with an interface, yield surface appears. The constitutive equation (1) shows that a jump discontinuity in the shear stress occurs across the yield surface. To resolve such singularity, an exponential regularization in the viscosity function is considered by Papanastasiou (1987). This adopted regularization method consists of an additional parameter m so that the modified equation is converted into a smooth function valid for the entire domain. The relation between shear stress and rate of strain is explicated as (Papanastasiou, 1987)

$$\tau^* = \left[\eta + \frac{{\tau_0}^*}{|\dot{\gamma}^*|}\{1 - exp(-m|\dot{\gamma}|)\}\right]\dot{\gamma}^* = \mu^*\dot{\gamma}^* \tag{2}$$

The dimensionless variables are defined by $x = x^*/H$, $y = y^*/H$, $t = t^*U_0/H$, $h = h^*/H$, $\theta = (T - T_c)/(T_h - T_c) = (T - T_c)/\Delta T$, $u = u^*/U_0$, $v = v^*/U_0$, $p = p^*/\rho_{nf}^* U_0^2$. φ_i is the local concentration of the ith type nanoparticles, which is scaled by the bulk concentration φ_{b_i}, i.e. $\varphi_i = \varphi_i^*/\varphi_{b_i}$. Here, subscripts f, p_i, nf refer to the clear fluid, particles and the hybrid nanofluid, respectively. Both the base fluid and nanoparticles are in a thermal equilibrium state.

We consider two-dimensional mixed convection of the Bingham plastic nanofluid, which is subjected to an externally imposed magnetic field applied horizontally. Under the Boussinesq approximation, the thermal buoyancy term present in the momentum equation is expressed as $(\rho\beta)_{nf}(T - T_c)\,\mathbf{g} = \varphi_{b_1}\varphi_1\rho_{p_1} + \varphi_{b_2}\varphi_2\rho_{p_2} + (1 - (\varphi_{b_1}\varphi_1 + \varphi_{b_2}\varphi_2))\rho_f\{1 - \beta(T - T_c)\}\,\mathbf{g}$, which can be further reduced to $(1 - \varphi_b)\rho_f\beta_f(T - T_c) - (\rho_{p_1} + \rho_{p_2} - \rho_f)(\varphi_{b_1}\varphi_1 + \varphi_{b_2}\varphi_2 - \varphi_b)\,\mathbf{g}$ under the assumption of dilute concentration of nanoparticles and a suitable choice of the reference pressure field. The nondimensional form of the governing equations under the Boussinesq approximation can be expressed as follows (Alsabery *et al.*, 2019):

$$\frac{\partial u}{\partial x}+\frac{\partial v}{\partial y}=0 \tag{3}$$

$$\frac{\partial}{\partial t}\left(\frac{\rho_{nf}}{\rho_f}u\right)+u\frac{\partial}{\partial x}\left(\frac{\rho_{nf}}{\rho_f}u\right)+v\frac{\partial}{\partial y}\left(\frac{\rho_{nf}}{\rho_f}u\right)=-\left(\frac{\rho_{nf}}{\rho_f}\right)\frac{\partial p}{\partial x}$$
$$+\frac{1}{Re}\left[\frac{\partial}{\partial x}\left\{\frac{\mu_{nf}}{\mu_f}\left(2\mu_f\frac{\partial u}{\partial x}\right)\right\}+\frac{\partial}{\partial y}\left\{\frac{\mu_{nf}}{\mu_f}\left(\mu_f\left(\frac{\partial u}{\partial y}+\frac{\partial v}{\partial x}\right)\right)\right\}\right] \tag{4}$$

$$\frac{\partial}{\partial t}\left(\frac{\rho_{nf}}{\rho_f}v\right)+u\frac{\partial}{\partial x}\left(\frac{\rho_{nf}}{\rho_f}v\right)+v\frac{\partial}{\partial y}\left(\frac{\rho_{nf}}{\rho_f}v\right)=-\left(\frac{\rho_{nf}}{\rho_f}\right)\frac{\partial p}{\partial y}$$
$$+\frac{1}{Re}\left[\frac{\partial}{\partial x}\left\{\frac{\mu_{nf}}{\mu_f}\left(\mu_f\left(\frac{\partial u}{\partial y}+\frac{\partial v}{\partial x}\right)\right)\right\}+\frac{\partial}{\partial y}\left\{\frac{\mu_{nf}}{\mu_f}\left(2\mu_f\frac{\partial v}{\partial y}\right)\right\}\right]$$
$$+Ri\left[Nr\left(1-\sum_{i=1}^{2}\varphi_i\right)+\theta\right]+\frac{\sigma_{nf}}{\sigma_f}\frac{Ha^2}{Re}v \tag{5}$$

$$\frac{\partial}{\partial t}\left(\frac{(\rho C_p)_{nf}}{(\rho C_p)_f}\theta\right)+u\frac{\partial}{\partial x}\left(\frac{(\rho C_p)_{nf}}{(\rho C_p)_f}\theta\right)+v\frac{\partial}{\partial y}\left(\frac{(\rho C_p)_{nf}}{(\rho C_p)_f}\theta\right)=\frac{1}{Re\cdot Pr}$$
$$\left[\left\{\frac{\partial}{\partial x}\left(\frac{k_{nf}}{k_f}\frac{\partial\theta}{\partial x}\right)+\frac{\partial}{\partial y}\left(\frac{k_{nf}}{k_f}\frac{\partial\theta}{\partial y}\right)\right\}+\sum_{i=1}^{2}\frac{1}{Le_i}\left\{\frac{\partial\theta}{\partial x}\frac{\partial\varphi_i}{\partial x}+\frac{\partial\theta}{\partial y}\frac{\partial\varphi_i}{\partial y}\right\}+\sum_{i=1}^{2}\frac{1}{Le_i\cdot N_{BT_i}}\left\{\left(\frac{\partial\theta}{\partial x}\right)^2+\left(\frac{\partial\theta}{\partial y}\right)^2\right\}\right]+J\frac{\sigma_{nf}}{\sigma_f}v^2 \tag{6}$$

$$\frac{\partial\varphi_i}{\partial t}+u\frac{\partial\varphi_i}{\partial x}+v\frac{\partial\varphi_i}{\partial y}=\frac{1}{Re\cdot Sc_i}\left(\frac{\partial^2\varphi_i}{\partial x^2}+\frac{\partial^2\varphi_i}{\partial y^2}\right)+\frac{1}{Re\cdot Sc_i\cdot N_{BT_i}}\left(\frac{\partial^2\theta}{\partial x^2}+\frac{\partial^2\theta}{\partial y^2}\right) \tag{7}$$

The no-slip boundary condition ($u = 0, v = 0$) is imposed on the heated cavity walls ($\theta = 1$) along with the no-normal flux of nanoparticles i.e. $J_{p_i}.\mathbf{n} = 0$, $\mathbf{n}$ being the unit outward normal to the surface. This relation implies $\frac{\partial\varphi_i}{\partial y}+\frac{1}{N_{BT_i}}\frac{\partial\theta}{\partial n}=0$. At the inlet, a velocity profile of lower temperature is assumed i.e.

$$u=cos\lambda\,,v=sin\lambda\,,\theta=0,\frac{\partial\varphi_i}{\partial x}=-\frac{1}{N_{BT_i}}\frac{\partial\theta}{\partial x}$$

The outflow boundary conditions are considered as follows:

$$\frac{\partial u}{\partial x}=0,\frac{\partial v}{\partial x}=0,\frac{\partial \theta}{\partial x}=0,\frac{\partial \varphi_i}{\partial x}=0$$

The equation for the nanoparticle volume fraction (7) is governed by the convection, Brownian diffusion and thermophoresis. The flux due to Brownian diffusion is $J_{P,B_i} = -\rho_{p_i} D_{B_i} \nabla \varphi_i$ where D_{B_i} is the Brownian diffusion coefficient, $D_{B_i} = \frac{K_B T}{3\pi \mu_f d_{p_i}}$. The mass flux due to thermophoretic effect is $J_{P,T_i} = -\rho_{p_i} D_{T_i} \frac{\nabla T}{T}$ where D_{T_i} is the thermal diffusion coefficient, $D_{T_i} = 0.26 \frac{K_f}{K_{p_i}+2K_f} \frac{\mu_f \varphi_{b_i}}{\rho_f}$. Here K_f is the thermal conductivity of the base fluid and K_{p_i} with $i = 1, 2$ represents, respectively, the thermal conductivity of Al_2O_3 and Fe_3O_4 nanoparticles. We have considered a sufficiently dilute mixture of two types of nanoparticles so that the interactions of different species of nanoparticles and the effect of agglomeration of nanoparticles is neglected (Huminic and Huminic, 2018). For the two-phase model, Fe_3O_4 nanoparticles with volume fraction φ_{b_2} is added with Al_2O_3-nanofluid of bulk volume fractions φ_{b_1} with the ratio $\delta = \varphi_{b_1}/\varphi_{b_2}$ and sum $\varphi_b = \varphi_{b_1} + \varphi_{b_2}$ is the net volume fraction.

The dimensionless parameter Hartmann number, $Ha = B_0 H \sqrt{\sigma_f/\mu_f}$ measures the ratio between the electromagnetic force to the viscous force, Joule heating parameter $J = Ha^2 Ec/Re$, where $Ec = U_0^2/(T_h - T_c)C_{pf}$ is Eckert number involves the magnetic field. The Schmidt number $Sc^i = \mu_f/(\rho_f D_{B_i})$ represents the ratio of momentum diffusivity and Brownian diffusivity, whereas the Lewis number $Le^i = k_f/\{(\rho C_p)_f D_{B_i} \varphi_{b_i}\}$ measures the ratio of thermal diffusivity to the Brownian diffusivity and $Nr = \varphi_b(\rho_{p_i} - \rho_f)/\{\rho_f \beta_f \Delta T(1-\varphi_b)\}$ is the buoyancy ratio between the nanofluid and base fluid. $N_{BT_i} = \varphi_{b_i} D_{B_i}/(D_{T_i}\Delta T)$ denotes the relative performance of the Brownian diffusion to that of the thermophoretic diffusion.

The thermophysical properties of hybrid nanofluid are expressed in terms of the properties of the base fluid and the composed nanoparticles. We consider the base fluid to be a Bingham plastic liquid and both the base fluid and nanoparticles are in a thermal equilibrium state. We consider the thermophysical properties of the base fluid and nanoparticles the same as considered in several existing studies (Garoosi *et al.*, 2014; Hojjat *et al.*, 2011; Ouyahia *et al.*, 2017) and are provided in Table 1. Under the low volume fraction of nanoparticles consideration, the thermophysical properties of the hybrid nanofluids can be determined through the linear model (Shah *et al.*, 2020; Xu, 2019). In the nondimensional form, the effective density (ρ_{nf}) and the effective heat capacitance ($(\rho c_p)_{nf}$) of the hybrid nanofluids are expressed as (Rashad *et al.*, 2018):

Parameter	Al_2O_3	Fe_3O_4	Base fluid
c_p(J/kgK)	765	670	4179
ρ(kg/m^3)	3970	5200	997.1
k(W/mK)	40	6	0.6
β(K^{-1})	0.85×10^{-5}	1.67×10^{-5}	2.1×10^{-4}
$\mu \times 104$ (kgm^{-1} s^{-1})	–	–	695
dp (nm)	0.385	47	–

Table 1. Thermophysical properties of Al_2O_3 and Fe_3O_4 nanoparticles and base fluid at $T = 290K$

$$\rho_{nf} = \left(1 - \sum_{i=1}^{2} \varphi_{b_i} \varphi_i\right) \rho_f + \sum_{i=1}^{2} \varphi_{b_i} \varphi_i \rho_{p_i} \tag{8}$$

$$(\rho c_p)_{nf} = \left(1 - \sum_{i=1}^{2} \varphi_{b_i} \varphi_i\right) (\rho c_p)_f + \sum_{i=1}^{2} \varphi_{b_i} \varphi_i (\rho c_p)_{p_i} \tag{9}$$

The effective thermal conductivity of the nanofluid is determined through the Maxwell–Garnetts (MG) model (Maxwell, 1873):

$$\frac{k_{nf}}{k_f} = \frac{\dfrac{\sum_{i=1}^{2} k_{p_i \varphi_{b_i} \varphi_i}}{\sum_{i=1}^{2} \varphi_{b_i} \varphi_i} + 2k_f - 2k_f \sum_{i=1}^{2} \varphi_{b_i} \varphi_i + 2\sum_{i=1}^{2} \varphi_{b_i} \varphi_i k_{p_i}}{\dfrac{\sum_{i=1}^{2} k_{p_i \varphi_{b_i} \varphi_i}}{\sum_{i=1}^{2} \varphi_{b_i} \varphi_i} + 2k_f + k_f \sum_{i=1}^{2} \varphi_{b_i} \varphi_i - \sum_{i=1}^{2} \varphi_{b_i} \varphi_i k_{p_i}} \tag{10}$$

Based on the Brinkman (1952) model, the apparent viscosity of the hybrid viscoplastic nanofluid can be expressed as follows (Kefayati, 2015):

$$\mu_{nf} = \frac{1}{\left(1 - \sum_{i=1}^{2} \varphi_{b_i} \varphi_i\right)^{2.5}} \left[1 + \frac{B_n}{|\dot{\gamma}|} \{1 - exp(-M|\dot{\gamma}|)\}\right] \tag{11}$$

Here $Bn = \tau_0^* H / \eta U_0$ is the Bingham number, and $M = mU_0/H$ is the stress growth parameter. The parameter M is considered to be sufficiently large so that the equation holds uniformly for yielded and unyielded regions. In our computation, we have chosen $M = 10^4$ to obtain the results. We have also considered several other models for the thermal conductivity and viscosity of the nanofluid such as the Corcione model (Corcione, 2011), MG–Brinkman model (Brinkman, 1952), MG–Pak and Cho model (Pak and Cho, 1998) and Patel–Brinkman model (Patel *et al.*, 2006). As discussed later in this article, the MG–Brinkman model is found to be the most convenient, and the result obtained by this model does not deviate much from the other well-established models. A similar observation is also made in the experiential study by Mahian *et al.* (2016). Based on the experimental data for the Al_2O_3–Fe_3O_4 hybrid nanofluid, Sulgani and Karimipour (2019) proposed the following correlation for the thermal conductivity:

$$\frac{k_{nf}}{k_f} = 0.113x1.001^{\theta} (\varphi_1 + \varphi_2)^{0.376} + 0.921 \tag{12}$$

We have also tested our computed results based on this correlation and compared them with the results based on the MG-Brinkman model, which has been discussed later in this article.

We consider the following Maxwell (1873) model for the electric conductivity, which is justified in the present study due to the consideration of dilute suspension of nanoparticles

$$\frac{\sigma_{nf}}{\sigma_f} = 1 + \frac{3\left(\frac{\sum_{i=1}^{2}\sigma_{p_i}\varphi_{b_i}\varphi_i}{\sigma_f} - \sum_{i=1}^{2}\varphi_{b_i}\varphi_i\right)}{\left(\frac{\sum_{i=1}^{2}\sigma_{p_i}\varphi_{b_i}\varphi_i}{\sigma_f\sum_{i=1}^{2}\varphi_{b_i}\varphi_i} + 2\right) - \left(\frac{\sum_{i=1}^{2}\sigma_{p_i}\varphi_{b_i}\varphi_i}{\sigma_f} - \sum_{i=1}^{2}\varphi_{b_i}\varphi_i\right)}. \tag{13}$$

The average Nusselt number Nu_{av} is obtained by integrating the local Nusselt number along the heated side walls normalized by the length of the side walls. The local entropy generated due to heat transfer irreversibility and fluid friction irreversibility, including the effect of the imposed magnetic field, is as follows:

$$S_{gen} = \frac{k_{nf}}{k_f}\left[\left(\frac{\partial\theta}{\partial x}\right)^2 + \left(\frac{\partial\theta}{\partial y}\right)^2\right] + \chi\left[\frac{\mu_{nf}}{\mu_f}\left\{2\left(\frac{\partial u}{\partial y}\right)^2 + 2\left(\frac{\partial v}{\partial x}\right)^2 + \left(\frac{\partial u}{\partial x} + \frac{\partial v}{\partial y}\right)^2\right\} + Ha^2\frac{\sigma_{nf}}{\sigma_f}v^2\right] \tag{14}$$

The irreversibility factor χ is determined by $\chi = \frac{\mu_f T_0 U_0^2}{k_f(\Delta T)}$. Here $T_0 = (T_h + T_c)/2$ is the reference temperature. The total entropy generation S_{av} is determined by integrating S_{gen} over the whole computational domain V divided by the total volume of the domain.

2.1 Heat function and energy flux vector

The energy flux vectors are locally tangential to the heat lines. It provides a correct visualization of the convective heat transfer and does not require to solve the Poisson equation for heat function (Costa, 2006). The energy flux vectors are defined as follows:

$$-\frac{\partial H}{\partial x} = RePr\frac{(\rho C_p)_{nf}}{(\rho C_p)_f}\theta v - \frac{k_{nf}}{k_f}\frac{\partial\theta}{\partial y}, \quad \frac{\partial H}{\partial y} = RePr\frac{(\rho C_p)_{nf}}{(\rho C_p)_f}\theta u - \frac{k_{nf}}{k_f}\frac{\partial\theta}{\partial x}$$

Here $H(x, y)$ is the heat function, which satisfies the energy equation identically. The net energy flow through the fluid is locally parallel to the heat lines $H(x, y) =$ constant. To avoid the complexity in determining the heat function, several authors have obtained the energy flux vector $\mathbf{E}$, locally tangential to the heatlines, defined as Pal *et al.* (2018):

$$\mathbf{E} = \left(\frac{\partial H}{\partial y}, -\frac{\partial H}{\partial x}\right)$$

2.2 Thermal mixing and temperature uniformity

The intensity of the thermal mixing inside the system is measured by computing θ_{cup} and θ_{av} known as mixing-cup temperature (θ_{cup}) and the velocity-weighted average temperature (θ_{av}), respectively. A better thermal mixing due to mixed convection is observed when the value of θ_{cup} and θ_{av} is higher. The mixing-cup temperature (θ_{cup}) and the volume-averaged temperature (θ_{av}) are defined as $\theta_{cup} = \frac{\int\int U^* \theta(x,y) dxdy}{\int\int U^* dxdy}$, $\theta_{av} = \frac{\int\int \theta(x,y) dxdy}{\int\int dxdy}$, where $U^* = \sqrt{u^2 + v^2}$

The significance of temperature uniformity within the nonhomogeneous system can be illustrated by computing the root mean square deviation (RMSD) of mixing-cup temperature and volume-averaged temperature are defined, respectively, as follows:

$$\theta^m_{cup} = \sqrt{\frac{\sum_{i=1}^{N} (\theta_i - \theta_{cup})^2}{N}}, \theta^m_{av} = \sqrt{\frac{\sum_{i=1}^{N} (\theta_i - \theta_{av})^2}{N}} \tag{15}$$

θ_i is the temperature at data point i. The smaller values of θ^m_{cup} and θ^m_{av} signify lower standard deviation indicating an improved temperature uniformity inside the enclosure.

3. Numerical methods

The governing nonlinear equations are discretized through the finite volume method over staggered grids. In the staggered grid arrangements, the computational domain is split up into a number of Cartesian cells. In each cell the scalar quantities such as pressure, temperature and the nanoparticles volume fraction are stored at the center, whereas the components of the velocity vectors are estimated at the midpoint of the corresponding sides of that cell to which they are normal. The diffusion terms in the equations are discretized by a second-order central difference type scheme based on the linear interpolation of variable values at either side of the cells. The temporal derivatives are discretized through the first-order implicit scheme. A third-order accurate upwind scheme, quadratic upwind interpolation for convective kinematics (QUICK) scheme (Hayase *et al.*, 1992), is adopted to approximate the convective terms in the momentum, energy and mass flux equations. The QUICK scheme imparts stability to the numerical scheme in the regions where a sharp change of variables occurs. The present mass-conservative numerical scheme has an overall second-order accuracy. A coupled correction of the pressure and velocity field is implemented through the pressure correction-based iterative technique, the SIMPLE (Fletcher, 2012) algorithm. In each iteration, the resulting block tri-diagonal system of linear algebraic equations is solved by a block elimination method. A detailed discussion on the discretization method is provided in Appendix 1.

We consider that the flow starts impulsively from rest and achieves a steady state after a transient phase. The time-dependent solutions are achieved by advancing the variables through a sequence of short time steps. At each time step, the iteration process starts with a known pressure field, which is upgraded iteratively by solving the Poisson equation for pressure correction. The iteration process is continued till the divergence-free velocity field is obtained. Based on the updated velocity field, the linearized momentum equations and other scalar transport equations are solved in a coupled manner. The convergence condition for the iteration is imposed as $\max_{ij} |\xi_{ij}^{(k+1)} - \xi_{ij}^{(k)}| \leq 10^{-5}$, ξ corresponds to the variables

u, v, θ or φ at any time step. Here, i, j denotes the cell index, and superscript k is the index for the iteration.

4. Grid independency test and code validation

We consider a uniform grid distribution along the x- and y-direction [Figure 1(b)]. An initial estimate of the grid is determined by comparing it with several existing results. A grid independence examination is performed to analyze the stability of the present numerical scheme, and an optimal grid distribution is determined for a cost-effective computation. The variation of grid size on the local Nusselt number is presented in Figure 2(a). The nondimensional quantity such as Nu is governed by the computed solution for the thermal field in the entire domain, which is coupled with the velocity field and nanoparticles distribution. The grid independency test is performed by considering four sets of grids, namely, 90×90, 150×150, 210×210 and 270×270, with the first number corresponding to the grids along the x-direction and the second number for the grids along the y-direction. For 90×90 grids, the grid size is $dx = dy = 0.004$ along with the horizontal and vertical directions. Modifying the grids from 90×90 to 150×150 creates a maximum difference of 0.18%, which reduces to 0.037% on further refinement i.e. 210×210 grids. Further refinement does not produce any significant change. The grid independence test suggests that 210×210 is the optimum grid size for our computational domain. The computer code is executed in the IBM Power 8 server, and the typical runtime for execution varies between 2 and 3 h with 99% central processing unit as the parameters such as Re or Ri vary.

A comparative study between several thermal conductivity and viscosity models for the nanofluid is assessed in Figure 2(b) by computing Nu_{av} at $Re = 100$, $Gr = 10^4$ and $Bn = 1$. It is evident that the MG–Brinkman model (Brinkman, 1952), Corcione model (Corcione, 2011) and the MG–Pak and Cho model (Pak and Cho, 1998) yields almost the same values, whereas the Patel–Brinkman model (Patel *et al.*, 2006) deviates from these models by a relatively larger margin. In the present study, we adopt the widely accepted MG–Brinkman model (Brinkman, 1952) to compute the effective viscosity and the thermal conductivity of the nanofluid. An experimental study by Mahian *et al.* (2016) also established that MG–Brinkman is appropriate to determine the thermal conductivity and viscosity of the nanofluid at a low volume fraction and produce a higher accuracy for heat transfer coefficient compared with other models.

In Figure 2(c), we made a comparison of our computed solution for the temperature profile at different values of the yield stress parameter Bn with the experimental results of Hassan *et al.* (2020) for the natural convection of the Bingham plastic clear

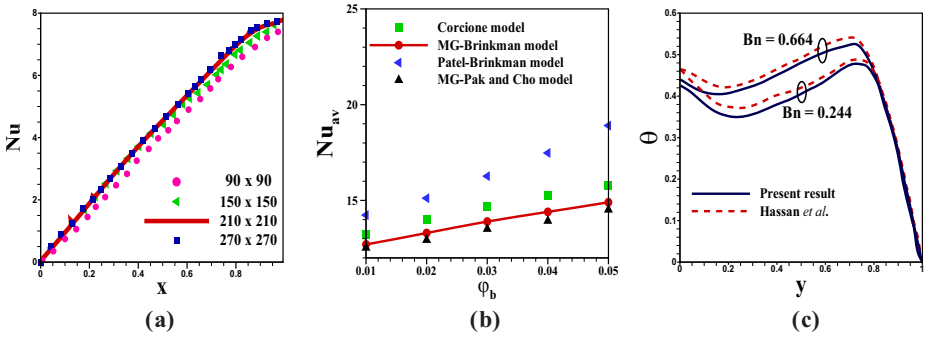

Figure 2.
(a) Grid independency test on Nu along the lower wall at different grid sizes when $Ri = 1$, $Bn = 10$, $Re = 100$ and $\varphi_b = 0.01$; (b) comparison of Nu_{av} obtained by several thermal conductivity and viscosity models at $Gr = 10^4$, $Re = 100$, $Ca = 1$, $Pn = 1$ for $\varphi_b = 0.01$; (c) comparison of temperature profile along the vertical axis at $x = 0.2$ and $Ra = 2.3 \times 10^5$ with experimental results of Hassan *et al.* (2020) for natural convection with $\varphi_b = 0$, $Bn = 0.244, 0.664$

fluid ($\varphi_b = 0$) in a square enclosure with discrete heat flux at the lower wall. Hassan *et al.* (2020) used the Carbopol polymer, which exhibits the shear-thinning viscoplastic behavior. The Bingham number (Bn), the ratio of yield stress and viscous stress, is varied to obtain the dependency of yield stress on the heat transfer rate. Results show that our computational results are fairly in agreement with the results determined experimentally. The computed solution is also found to differ by 7% from this experimental data.

Figure 3(a)–(c) presents the validation of our code with the existing numerical results. Figure 3(a) shows the comparison of our results for the average Nusselt number (Nu_{av}) for the Al_2O_3–water Newtonian ($Bn = 0$) nanofluid in a ventilated enclosure with the corresponding numerical results of Sourtiji *et al.* (2014) as a function of the bulk volume fraction (φ_b) in the absence of magnetic field ($Ha = 0$) and established an excellent agreement with maximum percentile difference 1.23%. The results are computed by varying the Richardson number for different modes of convection, namely, shear dominated ($Ri < 1$) and buoyancy dominated ($Ri = 10$) flows. A comparison of the local Nusselt number for the viscoplastic Bingham nanofluid with the numerical results of Kefayati and Huilgol (2016) is presented in Figure 3(b) for different values of Bn. We find an excellent agreement between the present results with the numerical results of Kefayati and Huilgol (2016), with a maximum difference of 3.09%. In Figure 3(c), we compare the vertical velocity profile along the vertical central line for the MHD mixed convection of a clear Newtonian ($\varphi_b = 0$, $n = 1$, $\tau_0 = 0$) fluid within a lid-driven square enclosure having two corner heaters placed along the bottom and right wall of width as half of the length of the wall with the numerical results of Oztop *et al.* (2011) for different values of the magnetic field (Ha). Results show an excellent agreement of our computed results with the existing numerical results.

5. Results and discussion

The hybrid nanofluid is considered to compose of δ: 1 ratio of Al_2O_3 and Fe_3O_4 nanoparticles with total bulk concentration φ_b. The governing nondimensional parameters such as Nr, Sc_i, Le_i and N_{BT_i} with $i = 1, 2$ corresponding to the nanoparticles Al_2O_3 and Fe_3O_4, respectively, are determined based on the intrinsic parameter values as prescribed in Table 1. For the sake of simplicity, the diameter of the two different types of nanoparticles is considered to be the same i.e.

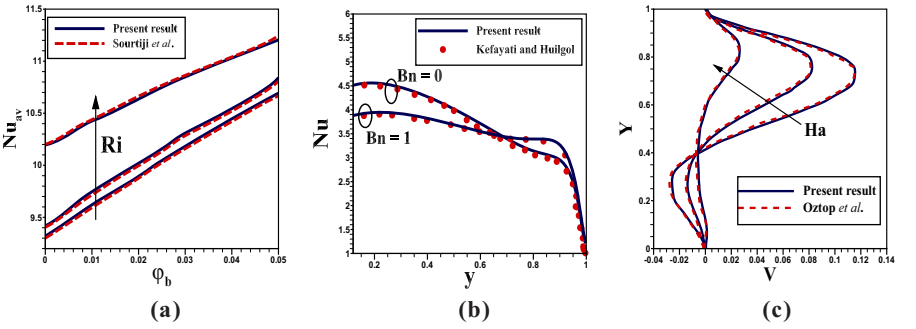

Figure 3.
(a) Comparison of Nu_{av} as a function of φ_b with Sourtiji *et al.* (2014) at different Ri (= 0.1, 1, 10) for mixed convection at $Re = 100$;
(b) comparison of Nu along the lower wall for $Bn = 0$ and 1 at $Re = 100$, $Pr = 1$ with Kefayati and Huilgol (2016) for $Bn = 0$ and 1 at $Re = 100$, $Pr = 1$;
(c) Comparison of vertical velocity profile along the y-axis i.e. $x = 0.5$ when $Re = 100$, $Gr = 10^4$, $\varphi_b = 0$ for $Ha = 0$, 10, 30 with numerical results of Oztop *et al.* (2011) for MHD mixed convection in a lid-driven square enclosure with corner heaters of length 0.5

$d_{p_1} = d_{p_2} = 30nm$. We first present the flow and thermal field for the mixed convection of the Bingham plastic hybrid nanofluid, which is followed by the results on heat transfer and entropy generation. Subsequently, the heat transfer efficiency and thermal mixing for the considered range of parameter values are illustrated.

5.1 Distribution of streamlines, heatlines and nanoparticles

The fluid pumped through the inlet placed at the top corner of the left side wall spreads inside the cavity and flows out through the lower corner of the opposite side wall. The flow pattern inside the cavity depends on the incoming fluid velocity (*Re*), wall temperature (*Gr*), bulk nanoparticles volume fraction (φ_{b_i}), Bingham number (*Bn*), Hartmann number (*Ha*) and the angle of inclination (λ) of the inlet jet. The flow, thermal field and the nanoparticles distribution along with the development of unyielded regions due to the presence of the horizontal jet of hybrid nanofluid in 1:1 ratio for different Bingham number (*Bn*) and Hartmann number (*Ha*) are presented in Figure 4(a)–(c). For the case of zero yield stress, the primary flow in the cavity constitutes of a cold fluid jet directed parallel to the diagonal direction of the cavity along with two viscous eddies of lower circulation strength developing near the lower and upper corners. For the case of nonzero yield stress ($Bn \neq 0$), the cold fluid jet flowing diagonally spreads and the corner eddies contract. For larger values of *Bn*, unyielded zones of stagnant fluid develop at both upper and lower corners of the cavity along with an unyielded region in which fluid moves as a solid body develops in the core of the cavity. Streamline patterns for larger *Bn* show symmetry about the diagonal line with unyielded regions formed symmetrically at the corners. An unyielded region develops in the bulk region where the fluid is not motionless rather moves like a solid body. The magnetic field interacts with the fluid at the bulk region in which the fluid experiences Lorentz force. In the presence of magnetic field unyielded regions, which develop at the corners shrinks and the fluid velocity in the vicinity of the walls become stronger. At a large value of *Ha* the streamlines spread throughout the domain so as to reduce the effect of the yield stress of the viscoplastic nanofluid.

The impact of the Bingham number, as well as the Hartmann number on the energy flux vector, is illustrated in the second row of Figure 4(a)–(c). The energy flux vectors are locally parallel to the direction of net energy flow in the convection field. It is seen that the vectors are directed along the diagonal in the core of the ventilated enclosure, which signifies that the heat transfer is strong in this region and is governed by the strong jet emanating from the inlet toward the outlet port. Away from the diagonal of the cavity, slower heat convection occurs, which leads to choose a longer path for the energy flux vectors to reach the outlet port. An increment of *Bn* diminishes the fluid convection due to the increment of viscosity of the nanofluid; hence, the heat transfer is dominated by conduction. For this, the circulation zones in the energy flux vectors reduce, and the flux vectors become parallel near the heated lower wall [Figure 4(b)]. The Lorentz force generated due to the imposed magnetic field affects the convective heat transfer phenomena within the bulk of the domain. It is evident from Figure 4(c) that as *Ha* increases, the heatlines follow a similar pattern like the streamlines. The heatlines are clustered near the heated walls so that the temperature gradient becomes steeper near the walls and the heat transportation between the cold fluid and the heated walls occurs at a higher rate.

The third row of Figure 4 shows the variation of nanoparticles distribution due to the increment of yield stress as well as the presence of Lorentz force at a fixed nanoparticle size

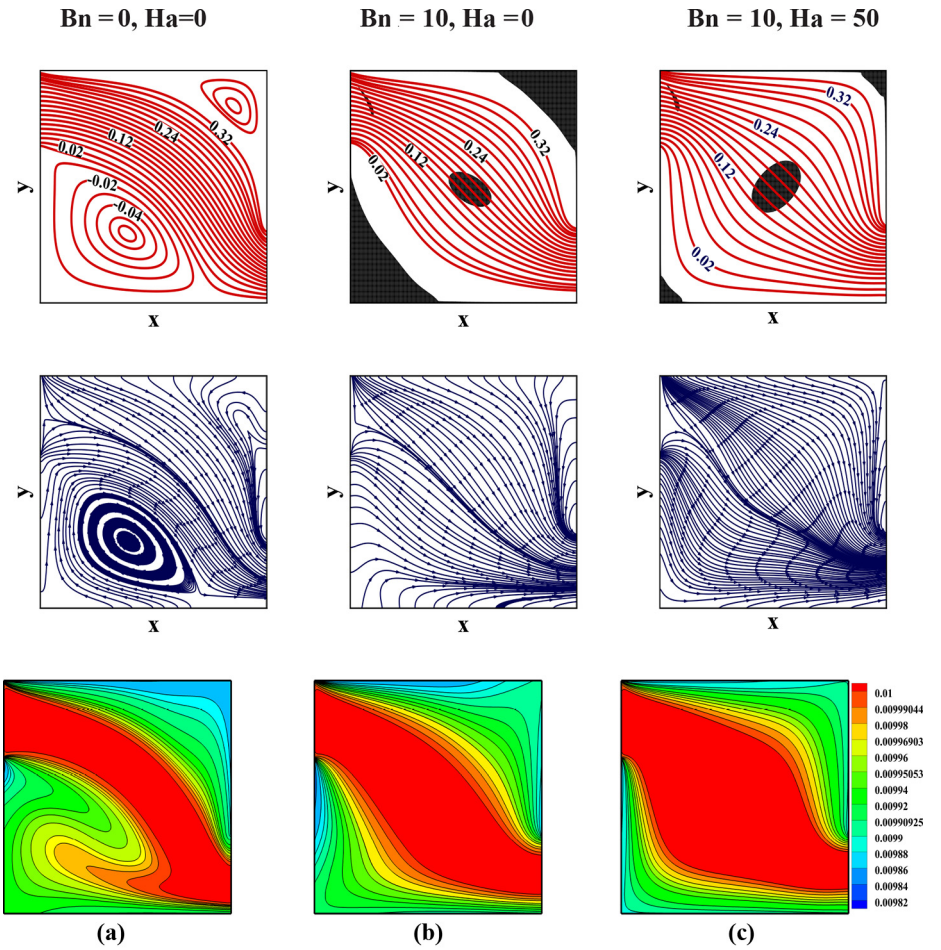

Figure 4.
Contour plot for streamlines and formation of unyielded regions (first row), heatlines (second row) and the nanoparticles distribution (third row) for (a) $Bn = 0, Ha = 0$; (b) $Bn = 10, Ha = 0$; (c) $Bn = 10, Ha = 50$ at $Ri = 1$, $\delta = 1$, $\varphi_b = 0.01$, $Re = 100$, $\lambda = 0^{\circ}$ and $\delta = 1$

Note: The unyielded regions correspond to $|\tau| \leq Bn$ marked as shaded regions

$d_{p_1} = d_{p_2} = 30\ nm$ and the sum of bulk volume fractions $\varphi_b = 0.01$, with 1:1 volume fraction ratio of two types of nanoparticles. Because the nonhomogeneous model considers a slip velocity between the base fluid and the nanoparticles, the impact of Brownian diffusion and thermophoresis is taken under consideration. Because the walls of the enclosure are maintained at a higher temperature, whereas the cold fluid flows along the diagonal, a comparatively higher concentration of nanoparticles is created near the inlet than the outlet port and a thin layer of low volume fraction nanoparticles is formed in the vicinity of the heated walls. Figure 4(b) shows that as the Bingham number enhances, the shape of the isoconcentration of nanoparticles is distorted. This is due to the fact that an increment in *Bn* causes a drop in the temperature gradient. For a higher value of *Bn*, the distribution of nanoparticles in the core becomes uniform as the increased yield stress reduces the convective transport of nanoparticles by enhancing the fluid viscosity and formation of

the unyielded region. It is evident from Figure 4(c) that the Lorentz force affects the nanoparticles distribution as *Ha* increases. The isoconcentration lines are contracted toward the wall of the enclosure leading to a faster change in the nanoparticle distribution near the wall.

5.2 Augmentation in heat transfer for hybrid nanofluid

A comparative study between the viscoplastic nanofluids composed of either Al_2O_3 ($\delta = \infty$) or Fe_3O_4 ($\delta = 0$) nanoparticles with the corresponding hybrid nanofluid ($\delta = 1$) consists of an equal proportion of Al_2O_3, and Fe_3O_4 nanoparticles are illustrated in Figure 5(a)–(c). It is evident from the results that the combination of Al_2O_3 and Fe_3O_4 nanoparticles produces higher heat transfer than the nanofluid composed of a single type of nanoparticles. The thermophysical properties such as thermal conductivity, viscosity, density and electric conductivity are being modified due to the inclusion of Fe_3O_4 nanoparticles with the Al_2O_3-nanofluid. It also improves the chemical stability of the hybrid nanofluid. Figure 5(a) shows that the enhancement in Nu_{av} for the hybrid nanofluid is pronounced at the higher range of Reynolds number. The presence of Fe_3O_4 particles in the nanofluid increases the shear rate, which becomes prominent for fluid at higher inertia i.e. higher Reynolds number. For higher values of the magnetic field, the hybrid nanofluid produces a substantial enhancement in Nu_{av}. This is due to the fact that the electrical conductivity of the Fe_3O_4 nanoparticles is higher, which manifests the impact of the magnetic field when Fe_3O_4 nanoparticles are considered i.e. $\delta > 0$. For the hybrid nanofluid, the increment of thermal conductivity is due to the chain formation of the magnetic nanomaterials with the base fluid, which intensifies with an increase of φ_b (Rashad *et al.*, 2018). It is evident that three types of nanofluids, i.e. $\delta = 0,1,\infty$ exhibits a similar pattern, however, a significant increment in Nu_{av} is observed for the case of hybrid nanofluid and the impact is pronounced for a higher value of *Re* due to strong convection.

Figure 5(b) depicts the impact of the inclination angle of the inlet jet on Nu_{av} for different values of the Bingham number. It is evident from the results that the maximum heat transfer is obtained at $\lambda = 0^{\circ}$ for all types of nanofluids. We find that the increment in yield stress (*Bn*) diminishes the rate of heat transfer. An increase in *Bn* enhances the fluid viscosity and also creates unyielded regions in the flow field. For this, the heat convection attenuates as *Bn* is increased. The discrepancy between the single nanofluid and the hybrid nanofluid reduces with the increase of *Bn* as the

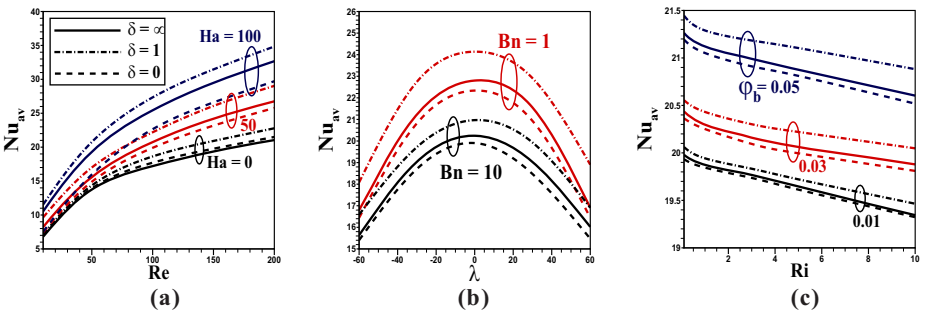

Figure 5. Comparative study on Nu_{av} for Fe_3O_4-nanofluid ($\delta = 0$, dashed lines), Al_2O_3-nanofluid ($\delta = \infty$, solid lines), Al_2O_3–Fe_3O_4 hybrid nanofluid ($\delta = 1$, dashed-dot lines) as a function of (a) *Re* at $Ri = 1$, $\lambda = 0^{\circ}$, $Bn = 10$, $\varphi_b = 0.01$; (b) λ at $Re = 100$, $Ri = 1$, $Ha = 50$, $\varphi_b = 0.01$; (c) *Ri* at $Re = 100$, $\lambda = 0^{\circ}$, $Bn = 10$, $Ha = 50$

impact of hybrid nanoparticles attenuates at higher yield stress, creating a large reduction in the convective heat transfer.

It is evident from Figure 5(c) that the rate of heat transfer augments due to the inclusion of Fe_3O_4 with the Al_2O_3 nanofluid i.e. $\delta = 1$. As mentioned before, the thermal conductivity of the hybrid nanofluid becomes higher than the nanofluid composed of a single type of particle. A significant influence of hybrid nanofluid compared with single nanofluids is observed for higher φ_b. We find that for all three types of fluids, an increment in Ri reduces Nu_{av} due to the formation of a secondary vortex, as discussed earlier. From Figure 5(a)–(c), it can be concluded that the hybrid nanofluid ($\delta = 1$) achieves a higher heat transfer rate than any of the viscoplastic nanofluids made of a single type of nanoparticles. For this, we consider the hybrid nanofluid in the rest of our computation to investigate the thermal performance of the system.

5.3 Heat transfer and entropy generation

Figure 6(a) shows the dependence of the average rate of heat transfer (Nu_{av}) on Ri at different values of the particle volume fraction composed of equal proportion of Al_2O_3 and Fe_3O_4 nanoparticles i.e. $\delta = 1$. We find that an increment in Ri causes a reduction in Nu_{av}. Here Ri is increased by increasing the temperature difference at a fixed Re. As observed from the flow and thermal field (Figure 4), an increase in Ri makes the region of primary flow squeeze, and as a result, the corner eddies expand. These vortices entrap fluid and refrain cold jet to spread near the heated walls, which, in turn, creates a monotonic decrement in the Nu_{av} with the increase of Ri. In the buoyancy-dominated regime i.e. at $Ri = 10$, two corner eddies appear with a sharp zone of a primary jet emanating along the diagonal direction. We find that an increment of the bulk volume fraction causes a notable enhancement in heat transfer determined by both the homogeneous and nonhomogeneous models. This inclusion of nanoparticles enhances the thermal conductivity of the nanofluid and modifies the thermal boundary layers. These effects manifest as φ_b is increased.

It is evident from Figure 6(a) and 6(b) that the nonhomogeneous model produces a higher heat transfer rate than the single-phase homogeneous model, and both models follow a similar trend as Ri or Re is varied. The Brownian diffusion and thermophoresis of the nanoparticles lead to an increment in heat transfer. The difference between the homogeneous and the nonhomogeneous model is 10.64% and

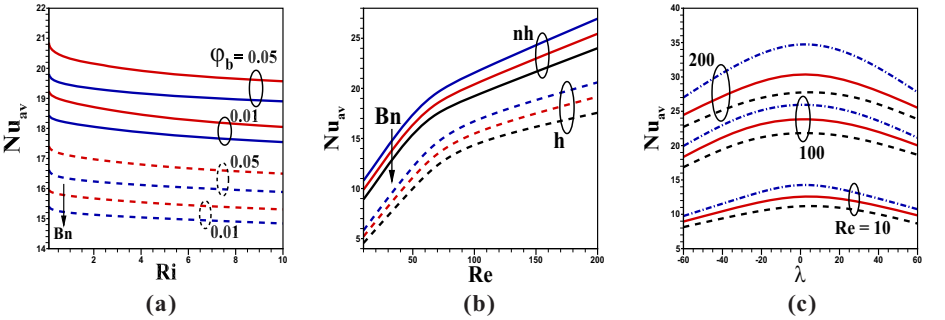

Figure 6.
Variation of Nu_{av} for the 1:1 Al_2O_3–Fe_3O_4-hybrid nanofluid ($\delta = 1$) with (a) Ri for different values of $Bn = 1$ (red lines), $Bn = 10$ (blue lines) and $\varphi_b = 0.01, 0.05$ at $\delta = 1, Re = 100, Ha = 0$ for the nonhomogeneous (solid line) and homogeneous (dashed line) model; (b) Re for $Bn = 1, 5, 10$ at $Ri = 1$, $\delta = 1$, $Ha = 0$ for the nonhomogeneous (solid line) and homogeneous (dashed line) model; (c) λ for different values of $Ha = 10$ (dashed lines), $Ha = 50$ (solid lines), and $Ha = 100$ (dashed-dotted lines) for the hybrid nanofluid at $Ri = 1, Bn = 10, \delta = 1$ and $\varphi_b = 0.01$

9.71% for φ_b = 0.01 and 0.05, respectively, at a fixed Ri (=10). The coefficient of the thermal buoyancy term in the nonhomogeneous model reduces as φ_b is increased, which leads to a reduction in Nu_{av} by a small margin compared with the homogeneous model. However, the discrepancy between the nonhomogeneous model and the results based on the single-phase model becomes pronounced as the Reynolds number is increased [Figure 6(b)]. At a higher Re, the dispersion of nanoparticles creates a higher thermal conductivity of the fluid, which is not accounted in the homogeneous model.

Figure 6(b) shows that an increment of the yield stress parameter Bn attenuates Nu_{av} for both the homogeneous and the nonhomogeneous models. An increase in yield stress creates a larger region of unyielded zones within the flow domain, which attenuates the fluid convection. We find that the reduction in Nu_{av} with the increment of Bn occurs at a slower rate for the lower range of Re. The maximum reduction in Nu_{av} when Bn is varied from 1 to 10 is 8.64% at Re = 200 while it is 7.23% at Re = 50. The disparity between the homogeneous and the nonhomogeneous models increases with the augmentation of the yield stress parameter Bn. The difference is 9.12% for Bn = 1, 9.94% for Bn = 5 and 10.65% for Bn = 10 at Re = 100. The variation of Nu_{av} at different Re with the inclination angle of the jet shows that Nu_{av} for any choice of Re achieves a local maximum at $\lambda = 0°$ [Figure 6(c)]. Because the inclined cold fluid jet creates vortices in the upper and lower corners and contracts the region of primary flow, it inhibits the interactions of the cold fluid with the heated sidewalls of the enclosure. At $\lambda = 0^{\circ}$ (horizontal jet), the main flow covers the entire domain, leading to an augmented heat transfer. A similar conclusion has also been established by Shiriny *et al.* (2019) based on the Newtonian fluid. The results show that the rate of enhancement in Nu_{av}, with the increment in Re, is faster for a positive inclination angle. The imposed transverse magnetic field, acting in the opposite direction of the injected jet, increases Nu_{av}, and this augmentation in Nu_{av} is pronounced at higher Re. At a higher Reynolds number, the heat transfer is dominated by forced convection. For this, the impact of Ha on Nu_{av} becomes pronounced for a higher range of Re. Heat transfer augmentation by imposing an external magnetic field in the mixed convection of a *ZnO*-viscoplastic nanofluid in ventilated cavities is also found by Kherroubi *et al.* (2020). The horizontal injection of the cold fluid provides maximum heat transfer at any value of Ha as the fluid convection in the bulk region becomes stronger for $\lambda = 0°$.

The dependency of Nu_{av} on the magnetic field for different values of Ri and Bn is presented in Figure 7(a). The average Nusselt number enhances monotonically with the

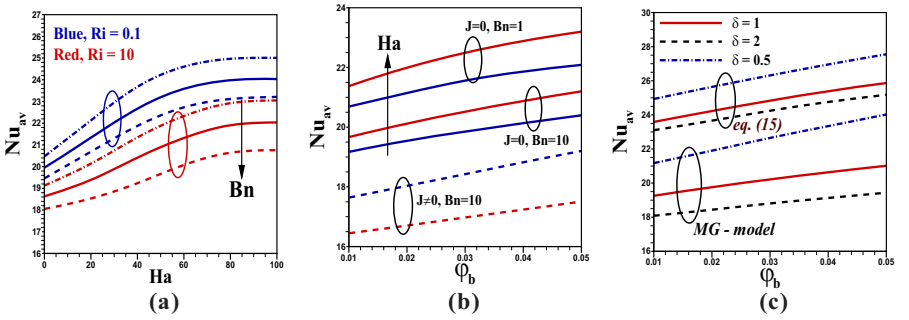

Figure 7.
Variation of Nu_{av} with (a) Ha for Bn = 0 (dashed-dotted lines), Bn = 1 (solid lines) and Bn = 10 (dashed lines) and Ri (= 0.1, 10) at φ_b = 0.01, Re = 100, δ = 1; (b) φ_b for Ha = 50 (blue lines), and Ha = 100 (red lines) at Re = 100, Ri = 1, Bn = 1, 10, φ_b = 0.01 with J = 0 (solid lines) and different J (dashed lines) at Ec = 0.1; (c) φ_b for different thermal conductivity model i.e. the MG-model and correlation (19) for δ = 0.5 (dashed-dotted lines), δ = 1 (solid lines) and δ = 2 (dashed lines) at Ha = 50, Bn = 10, Ri = 1

increment of Ha and achieves a saturation at a large Ha i.e. $Ha > 80$. As is seen from the streamline pattern, the imposed magnetic field induced Lorentz force acts in the supporting direction to the cold fluid emerging from the inlet. The corner eddies are diminished, and the cold fluid emanating from the inlet spreads throughout the domain. This leads to an increment in heat transfer as Ha is increased. It is observed that the impact of Ha is pronounced for lower values of Bn as the fluid convection attenuates at a higher Bn. The reduction of Nu_{av} with the increase of Bn in MHD mixed convection of viscoplastic fluids in a lid-driven cavity is also found by Kefayati and Tang (2018). With the increment of bulk volume fraction, the thermal conductivity manifests, and the thermal boundary layer modifies as well, which leads the Nu_{av} to increase monotonically with the increase of φ_b.

Figure 7(b) presents the effect of Joule heating on Nu_{av} at a fixed Ha. The Joule heating is generated due to the interaction of the electric current produced by the imposed magnetic field on the conducting fluid medium. It converts the kinetic energy into thermal energy, which leads to an increment in the fluid temperature. Because Joule heating enhances the fluid temperature leading to a thickening of the thermal boundary layer, and hence, it attenuates the wall temperature gradient i.e. a decrease of Nu_{av}. We find that the impact of Joule heating on Nu_{av} is pronounced for a higher range of Bn. The Joule heating parameter causes a decrement in conduction, whereas the convection is reduced due to the increment of yield stress (Bn). Both in combination creates an overall reduction in the heat transfer rate. The fact that the impact of Ha is pronounced for $J = 0$ is also evident from the figure. We find that the effect of the magnetic field is pronounced for a higher nanoparticles concentration as the electrical conductivity of the nanofluid manifests with φ_b.

We have compared Nu_{av} determined by the present model with the results based on the experimental correlation for thermal conductivity (12) in Figure 7(c) for a different proportion of the hybrid nanoparticles i.e. $\delta = 0.5, 1, 2$. We find that the results based on these two models are qualitatively similar. However, the results based on the correlation (12) produce a higher Nu_{av}. It is evident that Nu_{av} for the hybrid nanofluid augments with the reduction of δ i.e. as the percentage of Fe_3O_4 becomes higher than the Al_2O_3 nanofluid. The inclusion of Fe_3O_4 nanoparticles enhances the electrical conductivity of the medium, leading to an enhanced thermal performance when subjected to an imposed magnetic field. This impact of the applied magnetic field enhances as the relative volume fraction of Fe_3O_4 is increased. As a result, the hybrid composition with a 1:2 ratio ($\delta = 0.5$) achieves a higher rate of heat transfer.

The variation of the total entropy generation with the governing thermophysical parameters are presented in Figure 8(a)–(c). The entropy generation is governed by the

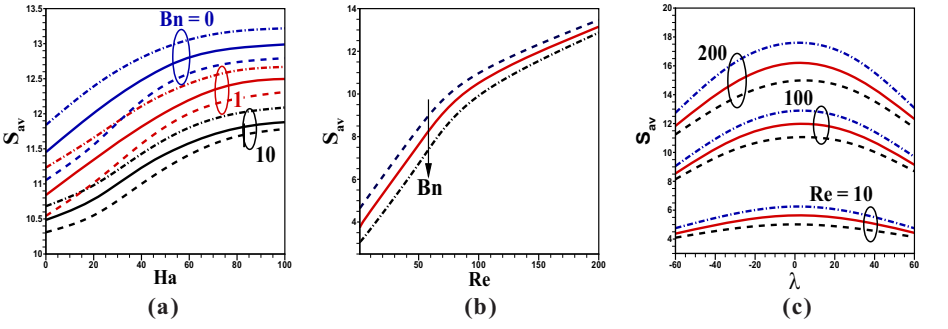

Figure 8.
Variation of S_{av} for hybrid nanofluid with $\delta = 1$ as a function of (a) Ha for different $Ri = 0.1$ (dashed lines), $Ri = 1$ (solid lines) and $Ri = 10$ (dashed-dotted lines) and Bn (0, 1, 10) at $\varphi_b = 0.01$, $Re = 100$, $\delta = 1$; (b) Re for Bingham number $Bn = 1, 5, 10$ at $Ri = 1$, $\delta = 1$, $Ha = 0$; (c) λ for different values of $Ha = 10$ (dashed lines), $Ha = 50$ (solid lines) and $Ha = 100$ (dashed-dotted lines) at $Ri = 1$, $Bn = 10$ and $\varphi_b = 0.01$

combined contribution of heat transfer irreversibility and fluid friction irreversibility due to the shear and buoyancy force for the present mixed convection flow of hybrid nanofluid. Because the average Bejan number is higher than 0.5, the heat transfer irresistibility dominates in generating the entropy. Figure 8(a) demonstrates that the total entropy generation enhances with the increment of *Ha* as the Lorentz force but declines with the increase of the Bingham number. An enhancement in Bingham number leads to a drop in entropy generation as both the fluid friction and heat transfer irresistibility reduces as *Bn* is increased. An increase in yield stress of the fluid elongates the unyielded regions in the flow domain where shear stress is low and also reduces the heat transfer due to convection. These, in combination, reduce S_{av} as *Bn* is increased. We have seen in Figure 7(a) that the average heat transfer reduces with the increase of *Ri*; however, S_{av} is increased as *Ri* increases. This implies that the fluid friction irreversibility due to shear stress contributes significantly to entropy generation for the buoyancy-dominated flow ($Ri > 1$). When Joule heating is considered, the temperature gradient attenuates due to an increase in fluid temperature, which leads to a reduction in entropy generation.

Figure 8(b) shows that an enhancement in *Re* increases S_{av}. An increase in *Re* increases the convective heat transfer as well velocity gradient due to faster change in velocity. Figure 8(c) shows that the variation of S_{av} with λ follows a similar pattern as the Nu_{av} variation, and the optimal entropy generation is obtained at $\lambda = 0°$, at which the maximum heat transfer is determined. The impact of λ is pronounced for higher values of *Re*, for which the inertia force dominates.

The dependency of entropy generation on Richardson number, nanoparticles concentration and Joule heating parameter at different Reynolds numbers is shown in Figure 9(a)–(c). Figure 9(a) shows that S_{av} increases as the volume fraction of the hybrid nanofluid are increased. An increment in φ_b enhances the temperature gradient as well as fluid friction, which in turn enhances S_{av}. As expected, an increase in *Ri* decreases S_{av}, and the variation of S_{av} with *Ri* is similar for any nonzero *Bn*. It is depicted from Figure 9(b) that in the presence of a magnetic field, the heat transfer irreversibility is higher for the Fe_3O_4 nanofluid ($\delta = 0$), and it becomes lower for Al_2O_3 nanofluid ($\delta = \infty$). We find that the addition of Al_2O_3 nanoparticles with the Fe_3O_4-nanofluid reduces the S_{av} compared with the case of Fe_3O_4-nanofluid. For the hybrid nanofluid ($\delta = 1$), the irreversibility in comparison with the Fe_3O_4-nanofluid ($\delta = 0$) is reduced due to the fact that the irreversibility attenuates as the electrical conductivity of the hybrid nanofluid becomes lower with the increment of volume relative fraction (δ) of the Al_2O_3 nanoparticles. The Joule heating decreases S_{av} by

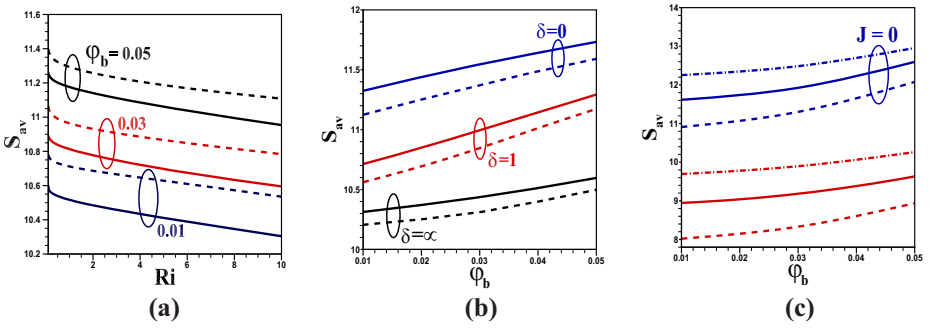

Figure 9. Variation of S_{av} for hybrid nanofluid with $\delta = 1$ as a function of (a) *Ri* for different values of *Bn* = 1 (dashed lines), *Bn* = 10 (solid lines) for $\varphi_b = 0.01, 0.05$, *Re* = 100, $\delta = 1$, *Ha* = 0; (b) φ_b for different $\delta = 0, 1, \infty$ and *Bn* = 1 (solid lines), 10 (dashed lines) at *Re* = 100, *Ri* = 1, *Ha* = 50; (c) φ_b for different values of *Ha* = 10 (dashed lines), *Ha* = 50 (solid lines), and *Ha* = 100 (dashed-dotted lines) at *Re* = 100, *Ri* = 1, *Bn* = 10, $\varphi_b = 0.01$ with $J = 0$ (blue lines) and different *J* (Red lines) at *Ec* = 0.1 using the nonhomogeneous model

the same mechanisms for which Nu_{av} is reduced. A monotonic increment in S_{av} with the enhancement of φ_b is observed [Figure 9(c)]. We find that the variation of S_{av} with φ_b is similar for any choice of *Ha*.

5.4 Enhancement of heat transfer with respect to entropy generation and pressure drop

Enhancement in heat transfer (E_h^{φ}) and the entropy generation (E_s^{φ}) due to the addition of Al_2O_3 and Fe_3O_4 nanoparticles in equal proportion ($\delta = 1$) are determined by $E_h^{\varphi} = Nu_{av}/Nu_{av}(\varphi_b = 0)$ and $E_S^{\varphi} = S_{av}/S_{av}(\varphi_b = 0)$, respectively. The dependency of E_h^{φ} and E_S^{φ} on the governing parameters, e.g. bulk volume fraction (φ_{b_i}), Richardson number (*Ri*), Reynolds number (*Re*) and Bingham number (*Bn*), are presented in Figure 10(a)–(c). Our results show that both the heat transfer and entropy generation augments due to the inclusion of two different types of nanoparticles for all the cases considered i.e. both E_h^{φ}, $E_S^{\varphi} > 1$. We also find that $E_h^{\varphi} > E_s^{\varphi}$ [inset of Figure 10(a)], which implies that the augmentation in heat transfer is higher than the loss due to entropy generation for all the cases considered. This is an important conclusion, which provides a guideline for designing optimal heat transfer for the ventilated enclosure.

A comparative study on the enhancement factors of heat transfer and entropy generation (E_h^{φ}, E_s^{φ}) between the hybrid nanofluid and Al_2O_3-nanofluid ($\delta = \infty$), as well as Fe_3O_4-nanofluid ($\delta = 0$), is presented in Figure10(a). It is evident from the results that the enhancement in heat transfer is much higher than the increment factor of entropy generation. An inclusion of Fe_3O_4 nanoparticles within the Al_2O_3-viscoplastic nanofluid manifests thermal performance ($E_h^{\varphi} > E_s^{\varphi}$). The Fe_3O_4 nanoparticles being electrically conducting increases the heat transfer rate of the hybrid nanofluid for a higher value of *Ha*. For this, the applied magnetic field produces an augmentation in heat transfer as well as entropy generation for the hybrid nanofluid with E_h^{φ} much larger than E_s^{φ}. The physical reason for $E_h^{\varphi} > E_s^{\varphi}$ in hybrid nanofluid is due to the fact that the inclusion of Fe_3O_4 into the Al_2O_3-nanofluids does not change the viscosity of the medium significantly compared with the enhancement in thermal conductivity. This characteristic of the hybrid nanofluid in the presence of the magnetic field may provide the guideline to design a thermodynamically efficient composition of nanofluid, resulting in intensified heat transfer with diminished entropy generation. We find from Figure 10(b) that an

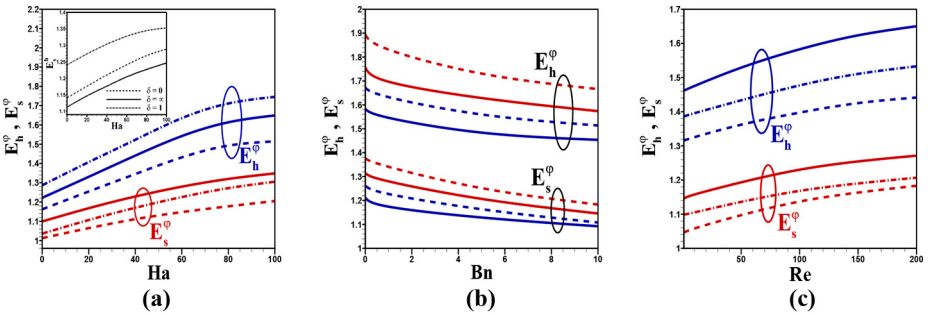

Note: Inset of (a) presents the ratio of heat transfer and entropy generation as a function of *Ha* for different δ

Figure 10.
Variation of E_h^{φ} and E_S^{φ} as a function of (a) *Ha* at a fixed *Ri* = 1, *Bn* = 10, $\varphi_b = 0.01$ for Fe_3O_4 nanofluid ($\delta = 0$, dashed lines), Al_2O_3 nanofluid ($\delta = \infty$, solid lines) and $Al_2O_3 - Fe_3O_4$ hybrid nanofluid ($\delta = 1$, dashed-dotted lines); (b) *Bn* for *Ri* = 0.1 (dashed lines) and *Ri* = 10 (solid lines) and $\varphi_b = 0.01$ (Blue lines) and $\varphi_b = 0.05$ (Red lines) at a fixed *Re* = 100, *Ha* = 50; (c) *Re* at $\varphi_b = 0.01$, *Ri* = 1 for *Bn* = 0, *Ha* = 0 (dashed-dotted lines), *Bn* = 10, *Ha* = 0 (dashed lines) and *Bn* = 10, *Ha* = 50 (solid lines), respectively

increment in yield stress creates an adverse effect on both $E_h^{\varphi}, E_s^{\varphi}$. The rate of increment in both the average Nusselt number and entropy generation attenuates as Bn is increased due to the adverse effect of yield stress.

Figure 10(c) shows that both the ratios E_h^{φ} and E_S^{φ} amplify as Re is increased. The development of unyielded regions in the Bingham plastic fluid attenuates the heat transfer, and this impact becomes pronounced at a larger Re. For the hybrid nanofluid, an imposition of the external magnetic field leads to an increment in both the enhancement factor for heat transfer and entropy generation; however, at a higher Re, the increment in E_h^{φ} is higher in comparison with the increment of E_s^{φ}.

The dimensionless pressure drop between the inlet and outlet port is defined as follows:

$$Pd = (P_{in} - P_{out})/(1/2)U_0^2\rho_f$$

P_{in} and P_{out} are the average pressure at inlet and outlet ports, respectively. We denote the enhancement in pressure drop due to the inclusion of nanoparticles as E_{Pd}^{φ} i.e. $E_{Pd}^{\varphi} = Pd/Pd^0$, where Pd^0 is the corresponding pressure drop for the case of $\varphi_b = 0$ (clear fluid). We define the ratio χ_{Pd}^h as $\chi_{Pd}^h = E_h^{\varphi}/E_{Pd}^{\varphi}$, which is the ratio in heat transfer enhancement compared with the enhancement in pressure drop due to the addition of nanoparticles. The results presented in Figure 11(a)–(c) show the variation of χ_{Pd}^h for different Ri and Re. Our results show that this computed ratio for all the cases is higher than 1. This implies that the inclusion of nanoparticles creates the rate of augmentation in heat transfer much higher than the enhancement of pressure drop between the nanofluid and clear fluid within the enclosure. The impact of the volume fraction of the nanoparticles in hybrid nanofluid on the ratio of enhancement χ_{Pd}^h is presented in Figure 11(a) at different Ri. An increment in bulk volume fraction of nanoparticles enhances the viscosity of the nanofluid, which causes a larger pressure drop compared with the clear fluid. However, the rate by which the heat transfer is enhanced is higher than the rate of increment in pressure drop, i.e. $E_h^{\varphi} > E_{Pd}^{\varphi}$. Although the enhancement in heat transfer diminishes with the increment of buoyancy force [inset of Figure 11(a)], the ratio χ_{Pd}^h of enhancement between the heat transfer and pressure drop compared with the clear fluid enhances with the increment of Ri [Figure 11(a)].

The effect of Re on the ratio of relative increment in heat transfer compared with the pressure drop due to the addition of nanoparticles is shown in Figure 11(b). An enhancement in Re leads to an increase in the Nu_{av} but declines the pressure drop. It is

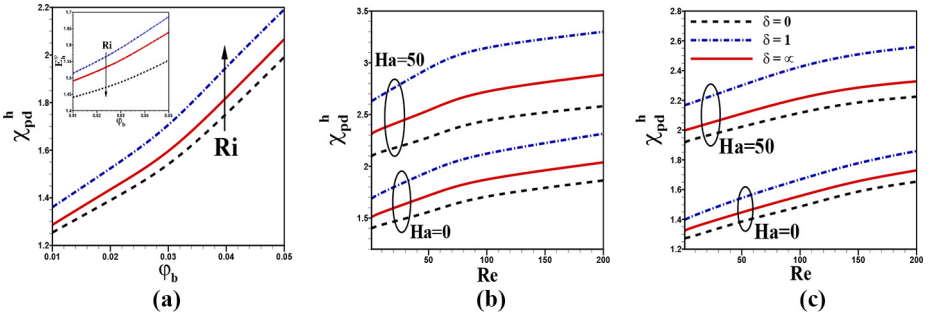

Figure 11. Variation of χ_{Pd}^h for Fe_3O_4/Al_2O_3 hybrid nanofluid (delta = 1) as a function of (a) φ_b for Ri (=0.1, 1, 10) at $Re = 100$, $Ha = 0$, $Bn = 10$. Inset shows the variation of E_h^{φ} as a function of φ_b for Ri (=0.1, 1, 10); (b) Re for $\varphi_b = 0.01, 0.03, 0.05$ with $Ha = 0$ (dashed lines), $Ha = 50$ (solid lines) at $Ri = 1$, $Bn = 10$. Variation of χ_{Pd}^h with (c) Re for $Ha = 0$, 50 for Fe_3O_4-nanofluid ($\delta = 0$, dashed lines), Al_2O_3-nanofluid ($\delta = \infty$, solid lines) and Fe_3O_4/Al_2O_3 hybrid nanofluid ($\delta = 1$, dashed-dotted lines) at $Ri = 1$, $Bn = 10$ and $\varphi_b = 0.01$

evident from the flow field that for lower values of *Re*, the primary flow expands in the core of the enclosure but contracts at the outlet port. This contraction of streamlines creates a significant enhancement in pressure drop near the outlet. However, the relative augmentation in heat transfer for nanofluid compared with the pressure drop is higher for the considered range of Reynolds number, and this ratio manifests with the increase of *Re*. The imposed magnetic field creates a larger pressure drop than the clear fluid i.e. E^{φ}_{Pd} becomes higher as *Ha* is increased. As the magnetic field pulls the nanoparticles toward the wall where the velocity is comparatively lower, the friction becomes higher near the wall, leading to an increment in pressure drop. This impact of the magnetic field on the pressure drop is suppressed in comparison with the heat transfer augmentation. For this, increment in *Ha* creates an enhancement in χ^{h}_{Pd}.

The ratio χ^{h}_{Pd} between the enhancement in heat transfer and pressure drop compared with the clear fluid for hybrid nanofluid as well as a single type of nanofluids is depicted in Figure 11(c). It is evident from the result that at the same volume fraction, the rate of heat transfer is higher than the pressure drop for the hybrid nanofluid compared with the corresponding single type of nanofluids. For the hybrid nanofluid, the enhancement in thermal conductivity is comparatively higher than the increment in viscosity. As a result $\chi^{h}_{Pd} > 1$ and it follows a similar pattern as that of Nu_{av} when varied as a function of *Re*.

5.5 Thermal mixing and temperature uniformity

The impact of the Bingham number on the buoyancy-dominated convection ($Ri = 10$) on the thermal mixing and temperature uniformity is shown in Figure 12(a) and 12(b). We find that both θ_{cup} and θ_{av} decrease with the increment of *Bn* [Figure 11(a) and 11(b)], which implies a reduction in thermal mixing for the viscoplastic nanofluid. The fluid convection reduces as the yield stress (*Bn*) is increased, which attenuates the thermal mixing. As shown before, an increment in *Ri* also reduces the primary flow domain and elongates the corner eddies. This creates an adverse effect on thermal mixing. We find that thermal mixing is enhanced due to the inclusion of nanoparticles due to enhanced thermal conduction. It is evident from Figure 12(a) and 12(b) that both θ_{cup} and θ_{av} increases with the increment of *Ha*. This implies a better thermal mixing due to the externally applied magnetic field for buoyancy-dominated convection.

The variation of θ^{m}_{cup} and θ^{m}_{av} Figure 12(a) and 12(b) indicates an augmentation in RMSD of mixing-cup temperature and volume-averaged temperature with the increment of Bingham number. This implies that the presence of viscoplastic nanofluid lessens the thermal mixing but enhances the temperature uniformity inside

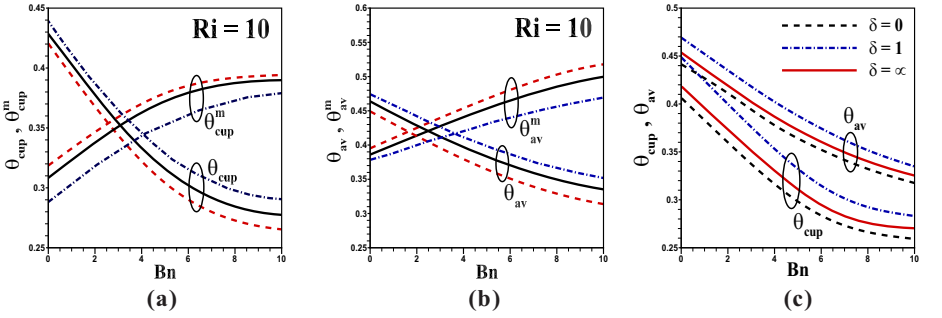

Figure 12.
Variation of (a) θ_{cup} and θ^{m}_{cup}; (b) θ_{av} and θ^{m}_{av} $Ri = 10$ as a function of *Bn* with $\varphi_b = 0.01$, $Ha = 0$ (dashed lines), $\varphi_b = 0.05$, $Ha = 0$ (solid lines), $\varphi_b = 0.05$, $Ha = 50$ (dashed-dotted lines) at a fixed at $Ri = 10$, $Re = 100$, $\delta = 1$; (c) θ_{cup} and θ_{av} with *Bn* for $\delta = 0$ (dashed lines), $\delta = \infty$ (solid lines), $\delta = 1$ (dashed-dotted lines) at $\varphi_b = 0.05$, $Ha = 50$, $Ri = 10$, $Re = 100$

the ventilated enclosure. It is evident from the results that the temperature nonuniformity is pronounced as the Hartmann number is increased. We find that the increment of nanoparticles concentration in the hybrid nanofluid has a marginal impact on the variation θ^m_{cup} and θ^m_{av}. Figure 12(c) depicts the impact of several nanofluids on the thermal mixing of the system. It is evident from the results that in the presence of a magnetic field, the thermal mixing is augmented in hybrid nanofluid ($\delta = 1$) in comparison with the single-particle nanofluids ($\delta = 0, \infty$).

6. Conclusion

A numerical investigation on the MHD mixed convection of a viscoplastic hybrid nanofluid in a ventilated enclosure with heated side walls is performed. Cold fluid is injected from the inlet at an angle λ with the horizontal, and an outlet is placed at the bottom corner of the opposite sidewall of the enclosure. The system is subjected to a uniform magnetic field imposed horizontally, acting opposite to the inlet jet. A nonhomogeneous model is adopted, which takes into account the relative velocity between the nanoparticles and the fluid. The governing equations are solved through the control volume-based algorithm. Comparison of the present model with the existing experimental results is encouraging. The impact of yield stress and magnetic field along with the Joule heating effect on the heat transfer performance of the hybrid nanofluid is analyzed. The main findings of the present study can be highlighted as follows:

- The difference between the nonhomogeneous and homogeneous models manifests as the yield stress is increased. This discrepancy between the two models becomes higher as the Reynolds number, Richardson number and nanoparticles volume fraction is increased.
- The hybrid nanofluid produces enhanced heat transfer with a lower rate of entropy generation and pressure drop than a nanofluid composed of a single type of nanoparticles. The inclusion of the $Al_2O_3 - Fe_3O_4$ hybrid nanoparticles on heat transfer performance manifests in the presence of the externally imposed magnetic field. Augmentation of heat transfer by 7.38% is achieved by 1:1 mixing of Al_2O_3 and Fe_3O_4 nanoparticles compared with the single Al_2O_3-nanofluid at Reynolds number $Re = 50$, whereas it is 16.61% at $Re = 200$.
- The rate of heat transfer diminishes with the increment of Richardson number as the region of the primary diagonal flow contracts, and the corner vortices elongate as the Richardson number is increases. The heat transfer becomes higher when the cold fluid is injected horizontally, and it reduces as the angle of inclination of the inlet jet deviates from horizontal.
- The yield stress of the fluid attenuates heat transfer by creating unyielded regions within the enclosures and increasing the viscosity of the fluid. The magnetic field acting opposite to the direction of the inward cold jet contracts the unyielded regions and produces an augmentation in heat transfer of the viscoplastic fluid.
- The Lorentz force generated due to the imposed magnetic field makes the fluid spread throughout the domain. This results in an enhanced heat transfer as well as a higher thermal mixing. The adverse effects on heat transfer due to the yield stress can be compensated by the applied magnetic field. The Joule heating induced by the imposed magnetic field increases the fluid temperature and consequently reduces the Nusselt number. Though the entropy generation increases with the increase of the strength of the magnetic field, the rate of enhancement remains lower than the rate by which the heat transfer is enhanced. Present results can serve as a useful tool in enhancing the heat transfer performance of a viscoplastic fluid in a ventilated enclosure.

References

Alsabery, A., Ismael, M., Chamkha, A. and Hashim, I. (2019), "Effects of two-phase nanofluid model on MHD mixed convection in a lid-driven cavity in the presence of conductive inner block and corner heater", *Journal of Thermal Analysis and Calorimetry*, Vol. 135 No. 1, pp. 729-750.

Arroub, I., Bahlaoui, A., Raji, A., Hasnaoui, M. and Naïmi, M., (2016), "Computational analysis of nanofluid mixed convection in a ventilated enclosure with linearly varying wall temperature", *Journal of Physical Science and Application*, Vol. 6 No. 6, pp. 49-56.

Bejan, A. (1980), "Second law analysis in heat transfer", *Energy*, Vol. 5 Nos 8/9, pp. 720-732.

Bianco, V., Diana, A., Manca, O. and Nardini, S. (2018), "Numerical investigation of an inclined rectangular cavity for ventilated roofs applications", *Thermal Science and Engineering Progress*, Vol. 6, pp. 426-435.

Bilgen, E. and Muftuoglu, A. (2008), "Cooling strategy by mixed convection of a discrete heater at its optimum position in a square cavity with ventilation ports", *International Communications in Heat and Mass Transfer*, Vol. 35 No. 5, pp. 545-550.

Brinkman, H. (1952), "The viscosity of concentrated suspensions and solutions", *The Journal of Chemical Physics*, Vol. 20 No. 4, pp. 571-571.

Buongiorno, J. (2006), "Convective transport in nanofluids", *Journal of Heat Transfer*, Vol. 128 No. 3, pp. 240-250.

Corcione, M. (2010), "Heat transfer features of buoyancy-driven nanofluids inside rectangular enclosures differentially heated at the sidewalls", *International Journal of Thermal Sciences*, Vol. 49 No. 9, pp. 1536-1546.

Corcione, M. (2011), "Empirical correlating equations for predicting the effective thermal conductivity and dynamic viscosity of nanofluids", *Energy Conversion and Management*, Vol. 52 No. 1, pp. 789-793.

Costa, V. (2006), "Bejan's heatlines and masslines for convection visualization and analysis", *Journal of Heat Transfer*, Vol. 59 No. 3, pp. 126-145.

Dogonchi, A.S., Armaghani, T., Chamkha, A.J. and Ganji, D. (2019b), "Natural convection analysis in a cavity with an inclined elliptical heater subject to shape factor of nanoparticles and magnetic field", *Arabian Journal for Science and Engineering*, Vol. 44 No. 9, pp. 7919-7931.

Dogonchi, A., Ismael, M.A., Chamkha, A.J. and Ganji, D. (2019a), "Numerical analysis of natural convection of Cu–water nanofluid filling triangular cavity with semicircular bottom wall", *Journal of Thermal Analysis and Calorimetry*, Vol. 135 No. 6, pp. 3485-3497.

Elelamy, A.F., Elgazery, N.S. and Ellahi, R. (2020), "Blood flow of MHD non-Newtonian nanofluid with heat transfer and slip effects", *International Journal of Numerical Methods for Heat and Fluid Flow*, Vol. 30 No. 11.

Ellahi, R., Alamri, S.Z., Basit, A. and Majeed, A. (2018), "Effects of MHD and slip on heat transfer boundary layer flow over a moving plate based on specific entropy generation", *Journal of Taibah University for Science*, Vol. 12 No. 4, pp. 476-482.

Ellahi, R., Sait, S.M., Shehzad, N. and Ayaz, Z. (2019), "A hybrid investigation on numerical and analytical solutions of electro-magnetohydrodynamics flow of nanofluid through porous media with entropy generation", *International Journal of Numerical Methods for Heat and Fluid Flow*, Vol. 30 No. 2.

Esfandiary, M., Mehmandoust, B., Karimipour, A. and Pakravan, H.A. (2016), "Natural convection of Al2O3–water nanofluid in an inclined enclosure with the effects of slip velocity mechanisms: Brownian motion and thermophoresis phenomenon", *International Journal of Thermal Sciences*, Vol. 105, pp. 137-158.

Esfe, M.H., Arani, A.A.A., Rezaie, M., Yan, W.-M. and Karimipour, A. (2015), "Experimental determination of thermal conductivity and dynamic viscosity of Ag–MgO/water hybrid

nanofluid", *International Communications in Heat and Mass Transfer*, Vol. 66, pp. 189-195.

Fletcher, C.A. (2012), *Computational Techniques for Fluid Dynamics 2: Specific Techniques for Different Flow Categories*, Springer Science and Business Media, New York, NY.

Garoosi, F., Garoosi, S. and Hooman, K. (2014), "Numerical simulation of natural convection and mixed convection of the nanofluid in a square cavity using Buongiorno model", *Powder Technology*, Vol. 268, pp. 279-292.

Ghalambaz, M., Doostani, A., Izadpanahi, E. and Chamkha, A.J. (2020a), "Conjugate natural convection flow of Ag–MgO/water hybrid nanofluid in a square cavity", *Journal of Thermal Analysis and Calorimetry*, Vol. 139 No. 3, pp. 2321-2336.

Ghalambaz, M., Mehryan, S., Zahmatkesh, I. and Chamkha, A. (2020b), "Free convection heat transfer analysis of a suspension of nano–encapsulated phase change materials (nepcms) in an inclined porous cavity", *International Journal of Thermal Sciences*, Vol. 157.

Gupta, S.K., Chatterjee, D. and Mondal, B. (2015), "Investigation of mixed convection in a ventilated cavity in the presence of a heat conducting circular cylinder", *Numerical Heat Transfer, Part A: Applications*, Vol. 67 No. 1, pp. 52-74.

Haik, Y., Pai, V. and Chen, C.-J. (2001), "Apparent viscosity of human blood in a high static magnetic field", *Journal of Magnetism and Magnetic Materials*, Vol. 225 Nos 1/2, pp. 180-186.

Hassan, M., Pathak, M., Khan, M.K. and Khan, N. (2020), "Natural convection of viscoplastic fluids in an enclosure with partially heated bottom wall", *International Journal of Thermal Sciences*, Vol. 158.

Hayase, T., Humphrey, J. and Greif, R. (1992), "A consistently formulated quick scheme for fast and stable convergence using finite-volume iterative calculation procedures", *Journal of Computational Physics*, Vol. 98 No. 1, pp. 108-118.

Heidary, H., Hosseini, R., Pirmohammadi, M. and Kermani, M. (2015), "Numerical study of magnetic field effect on nano-fluid forced convection in a channel", *Journal of Magnetism and Magnetic Materials*, Vol. 374, pp. 11-17.

Ho, C., Liu, W., Chang, Y. and Lin, C. (2010), "Natural convection heat transfer of alumina-water nanofluid in vertical square enclosures: an experimental study", *International Journal of Thermal Sciences*, Vol. 49 No. 8, pp. 1345-1353.

Hojjat, M., Etemad, S.G., Bagheri, R. and Thibault, J. (2011), "Rheological characteristics of non-Newtonian nanofluids: experimental investigation", *International Communications in Heat and Mass Transfer*, Vol. 38 No. 2, pp. 144-148.

Huminic, G. and Huminic, A. (2018), "Hybrid nanofluids for heat transfer applications – a state-of-the-art review", *International Journal of Heat and Mass Transfer*, Vol. 125, pp. 82-103.

Ingole, S. and Sundaram, K. (2016), "Experimental average nusselt number characteristics with inclined non-confined jet impingement of air for cooling application", *Experimental Thermal and Fluid Science*, Vol. 77, pp. 124-131.

Kefayati, G.R. (2015), "Mesoscopic simulation of mixed convection on non-Newtonian nanofluids in a two sided lid-driven enclosure", *Advanced Powder Technology*, Vol. 26 No. 2, pp. 576-588.

Kefayati, G. (2017), "Mixed convection of non-Newtonian nanofluid in an enclosure using Buongiorno's mathematical model", *International Journal of Heat and Mass Transfer*, Vol. 108, pp. 1481-1500.

Kefayati, G. (2018), "Double-diffusive natural convection and entropy generation of Bingham fluid in an inclined cavity", *International Journal of Heat and Mass Transfer*, Vol. 116, pp. 762-812.

Kefayati, G. and Huilgol, R. (2016), "Lattice boltzmann method for simulation of mixed convection of a Bingham fluid in a lid-driven cavity", *International Journal of Heat and Mass Transfer*, Vol. 103, pp. 725-743.

Kefayati, G.R. and Tang, H. (2018), "MHD mixed convection of viscoplastic fluids in different aspect ratios of a lid-driven cavity using LBM", *International Journal of Heat and Mass Transfer*, Vol. 124, pp. 344-367.

Khan, M.R., Pan, K., Khan, A.U. and Nadeem, S. (2020b), "Dual solutions for mixed convection flow of SiO2- Al2O3/water hybrid nanofluid near the stagnation point over a curved surface", *Physica A: Statistical Mechanics and Its Applications*, Vol. 547, p. 123959.

Khan, A.A., Naeem, S., Ellahi, R., Sait, S.M. and Vafai, K. (2020a), "Dufour and soret effects on Darcy-Forchheimer flow of second-grade fluid with the variable magnetic field and thermal conductivity", *International Journal of Numerical Methods for Heat and Fluid Flow*, Vol. 30 No. 9.

Kherroubi, S., Benkahla, Y.K., Labsi, N., Ragui, K., Bensaci, A., Boutra, A., Ouyahia, S.-E. and Benzema, M. (2020), "Two-and three-dimensional comparative study of heat transfer and pressure drop characteristics of nanofluids flow through a ventilated cubic cavity (part i: Newtonian nanofluids)", *Journal of Thermal Analysis and Calorimetry*, Vol. 1, pp. 1-24.

Koufi, L., Younsi, Z., Cherif, Y. and Naji, H. (2017), "Numerical investigation of turbulent mixed convection in an open cavity: effect of inlet and outlet openings", *International Journal of Thermal Sciences*, Vol. 116, pp. 103-117.

Ma, Y., Mohebbi, R., Rashidi, M. and Yang, Z. (2019), "MHD convective heat transfer of ag-mgo/water hybrid nanofluid in a channel with active heaters and coolers", *International Journal of Heat and Mass Transfer*, Vol. 137, pp. 714-726.

Mahian, O., Kianifar, A., Heris, S.Z. and Wongwises, S. (2016), "Natural convection of silica nanofluids in square and triangular enclosures: theoretical and experimental study", *International Journal of Heat and Mass Transfer*, Vol. 99, pp. 792-804.

Majee, S. and Shit, G. (2017), "Numerical investigation of MHD flow of blood and heat transfer in a stenosed arterial segment", *Journal of Magnetism and Magnetic Materials*, Vol. 424, pp. 137-147.

Maxwell, J.C. (1873), *A Treatise on Electricity and Magnetism*, 1. Clarendon Press: Oxford.

Mehmood, K., Hussain, S. and Sagheer, M. (2017), "Mixed convection in alumina-water nanofluid filled lid-driven square cavity with an isothermally heated square blockage inside with magnetic field effect: introduction", *International Journal of Heat and Mass Transfer*, Vol. 109, pp. 397-409.

Mehryan, S., Izadpanahi, E., Ghalambaz, M. and Chamkha, A. (2019), "Mixed convection flow caused by an oscillating cylinder in a square cavity filled with Cu-Al2O3/water hybrid nanofluid", *Journal of Thermal Analysis and Calorimetry*, Vol. 137 No. 3, pp. 965-982.

Mohammadi, M.-R. and Moghadam, A.J. (2015), "Heat transfer and entropy generation analysis of Bingham plastic fluids in circular microchannels", *Journal of Thermal Science and Engineering Applications*, Vol. 7 No. 4, pp. 041019-041011.

Nazari, S., Ellahi, R., Sarafraz, M., Safaei, M.R., Asgari, A. and Akbari, O.A. (2020), "Numerical study on mixed convection of a non-Newtonian nanofluid with porous media in a two lid-driven square cavity", *Journal of Thermal Analysis and Calorimetry*, Vol. 140 No. 3, pp. 1121-1145.

Ouyahia, S.-E., Benkahla, Y.K., Berabou, W. and Boudiaf, A. (2017), "Numerical study of the flow in a square cavity filled with carbopol-TiO_2 nanofluid", *Powder Technology*, Vol. 311, pp. 101-111.

Oztop, H.F., Al-Salem, K. and Pop, I. (2011), "MHD mixed convection in a lid-driven cavity with corner heater", *International Journal of Heat and Mass Transfer*, Vol. 54 Nos 15/16, pp. 3494-3504.

Pak, B.C. and Cho, Y.I. (1998), "Hydrodynamic and heat transfer study of dispersed fluids with submicron metallic oxide particles", *Experimental Heat Transfer an Transfer*, Vol. 11 No. 2, pp. 151-170.

Pal, S., Bhattacharyya, S. and Pop, I. (2018), "Effect of solid-to-fluid conductivity ratio on mixed convection and entropy generation of a nanofluid in a lid-driven enclosure with a thick wavy wall", *International Journal of Heat and Mass Transfer*, Vol. 127, pp. 885-900.

Papanastasiou, T.C. (1987), "Flows of materials with yield", *Journal of Rheology*, Vol. 31 No. 5, pp. 385-404.

Patel, H.E., Anoop, K., Sundararajan, T. and Das, S.K. (2006), "A micro-convection model for thermal conductivity of nanofluids", *International Heat Transfer Conference 13*, Begel House Inc.

Rashad, A., Chamkha, A.J., Ismael, M.A. and Salah, T. (2018), "Magnetohydrodynamics natural convection in a triangular cavity filled with a Cu-Al2O3/water hybrid nanofluid with localized heating from below and internal heat generation", *Journal of Heat Transfer*, Vol. 140 No. 7, pp. 072502-072501.

Rasool, G., Zhang, T., Chamkha, A.J., Shafiq, A., Tlili, I. and Shahzadi, G. (2020), "Entropy generation and consequences of binary chemical reaction on MHD Darcy – Forchheimer Williamson nanofluid flow over non-linearly stretching surface", *Entropy*, Vol. 22 No. 1, p. 18.

Sarkar, J., Ghosh, P. and Adil, A. (2015), "A review on hybrid nanofluids: recent research, development and applications", *Renewable and Sustainable Energy Reviews*, Vol. 43, pp. 164-177.

Shah, N.A., Animasaun, I., Wakif, A., Koriko, O., Sivaraj, R., Adegbie, K., Abdelmalek, Z., Vaidyaa, H., Ijirimoye, A. and Prasad, K. (2020), "Significance of suction and dual stretching on the dynamics of various hybrid nanofluids: comparative analysis between type i and type ii models", *Physica Scripta*, Vol. 95 No. 9.

Sheikhzadeh, G.A., Dastmalchi, M. and Khorasanizadeh, H. (2013), "Effects of nanoparticles transport mechanisms on alAO3–water nanofluid natural convection in a square enclosure", *International Journal of Thermal Sciences*, Vol. 66, pp. 51-62.

Sheremet, M.A., Pop, I. and Roşca, N.C. (2016), "Magnetic field effect on the unsteady natural convection in a wavy-walled cavity filled with a nanofluid: Buongiorno's mathematical model", *Journal of the Taiwan Institute of Chemical Engineers*, Vol. 61, pp. 211-222.

Shiriny, A., Bayareh, M. and Nadooshan, A.A. (2019), "Nanofluid flow in a microchannel with inclined cross-flow injection", *SN Applied Sciences*, Vol. 1 No. 9.

Sourtiji, E., Gorji-Bandpy, M., Ganji, D. and Hosseinizadeh, S. (2014), "Numerical analysis of mixed convection heat transfer of Al2O3-water nanofluid in a ventilated cavity considering different positions of the outlet port", *Powder Technology*, Vol. 262, pp. 71-81.

Sourtiji, E., Hosseinizadeh, S., Gorji-Bandpy, M. and Ganji, D. (2011), "Effect of water-based Al2O3 nanofluids on heat transfer and pressure drop in periodic mixed convection inside a square ventilated cavity", *International Communications in Heat and Mass Transfer*, Vol. 38 No. 8, pp. 1125-1134.

Sulgani, M.T. and Karimipour, A. (2019), "Improve the thermal conductivity of 10w40-engine oil at various temperature by addition of Al2O3/Fe2O3 nanoparticles", *Journal of Molecular Liquids*, Vol. 283, pp. 660-666.

Syrakos, A., Georgiou, G.C. and Alexandrou, A.N. (2013), "Solution of the square lid-driven cavity flow of a Bingham plastic using the finite volume method", *Journal of Non-Newtonian Fluid Mechanics*, Vol. 195, pp. 19-31.

Tayebi, T. and Chamkha, A.J. (2019), "Entropy generation analysis during MHD natural convection flow of hybrid nanofluid in a square cavity containing a corrugated conducting block", *International Journal of Numerical Methods for Heat and Fluid Flow*, Vol. 30 No. 3.

Varol, Y., Oztop, H.F. and Koca, A. (2008), "Entropy production due to free convection in partially heated isosceles triangular enclosures", *Applied Thermal Engineering*, Vol. 28 Nos 11/12, pp. 1502-1513.

Xu, H. (2019), "Modelling unsteady mixed convection of a nanofluid suspended with multiple kinds of nanoparticles between two rotating disks by generalized hybrid model", *International Communications in Heat and Mass Transfer*, Vol. 108.

Appendix. Discretization of the transport equations

The general form of the convective-diffusion equations for the generic variable C is follows:

$$\frac{\partial C}{\partial t}+\frac{\partial}{\partial x}(uc)+\frac{\partial}{\partial y}(vc)=\nabla^2 C+S_C \tag{16}$$

The computational domain is divided into a number of elementary sub-cells (Figure A1) with area V_p whose sides are dx_P and dy_P. Equation (16) is integrated over a cell V_p and the discretized form to advance the solution from nth time step to $(n+1)$th time step is as follows:

$$\begin{aligned}&\frac{C_P^{n+1}-C_P^n}{dt}\,dx_P\,dy_P+[u_eC_e-u_wC_w]^{n+1}dy_P+[v_nC_n-v_sC_s]^{n+1}dx_P\\&=\left[\left.\frac{\partial C}{\partial x}\right|_e-\left.\frac{\partial C}{\partial x}\right|_w\right]^{n+1}dy_P+\left[\left.\frac{\partial C}{\partial y}\right|_n-\left.\frac{\partial C}{\partial y}\right|_s\right]^{n+1}dx_P+(S_C)_P\,dx_P\,dy_P\end{aligned} \tag{17}$$

Here n, s, e and w refer to the northern, southern, eastern, western face of the cell (Figure A1). An implicit first-order scheme is used to discretize the time derivatives.

The diffusion flux at interfaces "e" and "w" are evaluated as follows:

$$\left.\frac{\partial C}{\partial x}\right|_e=\frac{C_E-C_P}{0.5(dx_P+dx_E)}\qquad\text{and}\qquad\left.\frac{\partial C}{\partial x}\right|_w=\frac{C_P-C_W}{0.5(dx_P+dx_W)}$$

A similar procedure is adopted to estimate the diffusion flux at the other cell faces "n" and "s". Note that the big letter subscripts denote the cell centers in which variables are stored, and small letter subscripts denote the corresponding cell faces.

To evaluate the value of C at the cell faces in the convective term, the QUICK scheme (Hayase *et al.*, 1992) has been used. The QUICK scheme is a three-point upstream-weighted quadratic interpolation for the convected property C at the cell faces. Thus, C_e and C_w at the cell faces can be obtained as follows:

$$C_e=\begin{cases}\frac{3}{8}C_E+\frac{3}{4}C_P-\frac{1}{8}C_W, & u_e>0,\\ \frac{3}{4}C_E+\frac{3}{8}C_P-\frac{1}{8}C_{EE}, & u_e<0;\end{cases}$$

$$C_w=\begin{cases}\frac{3}{8}C_P+\frac{3}{4}C_W-\frac{1}{8}C_{WW}, & u_w>0,\\ \frac{3}{4}C_P+\frac{3}{8}C_W-\frac{1}{8}C_E, & u_w<0;\end{cases}$$

Similarly, the values of C at interfaces "n" and "s" can be expressed. Therefore, the discretized equation (17) can be written as follows:

$$a_PC_P^{n+1}=a_EC_E^{n+1}+a_WC_W^{n+1}+a_NC_N^{n+1}+a_SC_S^{n+1}+a_P^0C_P^n \tag{18}$$

where the coefficients a_i ($i=E, W, P, N$ and S) are as follows:

$$a_E = D_e - \min(u_e, 0), \quad a_W = D_w + \max(u_w, 0),$$
$$a_N = D_n - \min(v_n, 0), \quad a_S = D_s + \max(v_s, 0),$$
$$a_P = D_e + \max(u_e, 0) + D_w - \min(u_w, 0) + \ D_n + \max(v_n, 0) + D_s - \min(v_s, 0) + a_P^0$$

with $a_P^0 = dx_P dy_P / dt$. The contribution of the diffusion terms is included in D_i ($i = E, W, P, N$ and S). Equation (18) is the discretized form of equation (16).

After discretization, the x- and y-momentum equations at the $(n + 1)$th time step for u and v, respectively, yields

$$\left.\begin{aligned} a_i^u u_{i-1,j}^{n+1} + b_i^u u_{i,j}^{n+1} + c_i^u u_{i+1,j}^{n+1} &= d_i^u - \left(p_{i+1,j}^{n+1} - p_{i,j}^{n+1}\right) \triangle y \\ a_i^v v_{i-1,j}^{n+1} + b_i^v v_{i,j}^{n+1} + c_i^v v_{i+1,j}^{n+1} &= d_i^v - \left(p_{i,j+1}^{n+1} - p_{i,j}^{n+1}\right) \triangle x \end{aligned}\right\} \tag{19}$$

The temperature and the nanoparticles concentration equations for at the $(n + 1)$th time step over the (i,j)th scalar control volume, we get

$$\left.\begin{aligned} a_i^f f_{i-1,j}^{n+1} + b_i^f f_{i,j}^{n+1} + c_i^f f_{i+1,j}^{n+1} &= d_i^f \\ a_i^g g_{i-1,j}^{n+1} + b_i^g g_{i,j}^{n+1} + c_i^g g_{i+1,j}^{n+1} &= d_i^g \end{aligned}\right\} \tag{20}$$

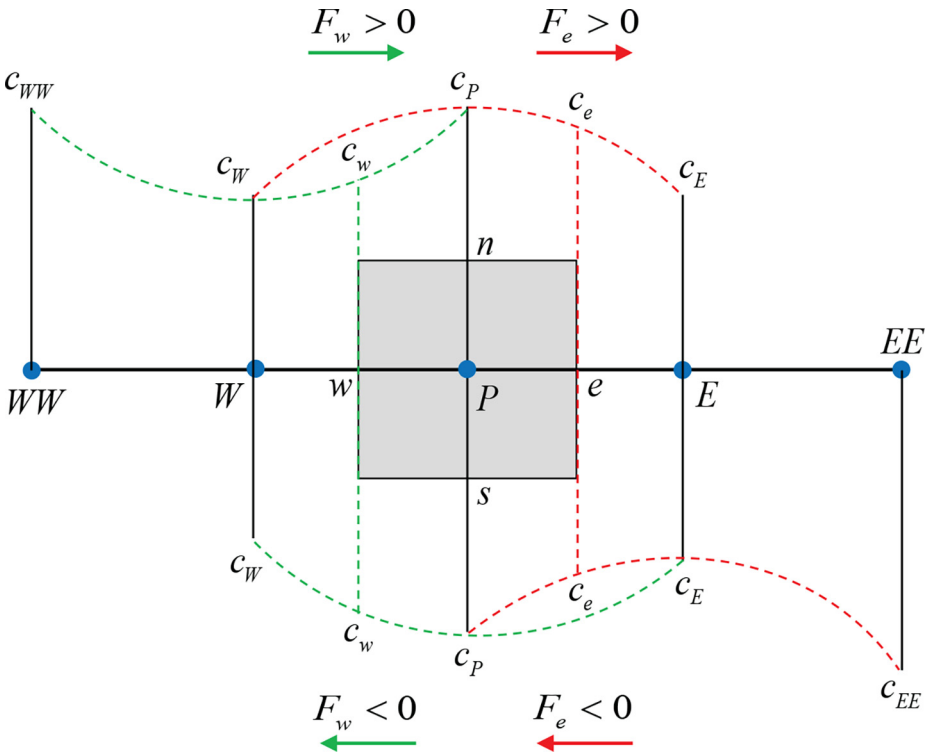

Figure A1. Schematic diagram for control volume V_P where e, w, n and s are the cell faces of the cell-centered at P

Here f stands for the temperature and g for nanoparticle concentration. For a fixed value of n, the system of equations can be expressed together in a matrix form as follows:

$$A_i X_{i-1}^{n+1} + B_i X_i^{n+1} + C_i X_{i+1}^{n+1} = D_i, \qquad i = 1, 2, \ldots, N \tag{21}$$

where $\left[X_i^{n+1}\right]^T = \left(u_{i,j}^{n+1}\ v_{i,j}^{n+1}\ f_{i,j}^{n+1}\ g_{i,j}^{n+1}\right)$ is the variable vector, A_i, B_i and C_i are the 4×4 coefficient matrices, and D_i is the known vector.

With these, the system of equations can be expressed in a block matrix form as follows:

$$\boldsymbol{AX} = \boldsymbol{D} \tag{22}$$

where

$$\boldsymbol{A} = \begin{pmatrix} B_1 & C_1 & & & \\ A_1 & B_1 & C_1 & & \\ & \ddots & \ddots & \ddots & \\ & & A_{n-1} & B_{n-1} & C_{n-1} \\ & & & A_n & B_n \end{pmatrix}$$

is a block tri-diagonal matrix, each element being a square matrix of order four, $\boldsymbol{X}$ being the vector of unknowns, and $\boldsymbol{D}$ is the vector of knowns. The linear system of equations is solved by using a block elimination algorithm.

Corresponding author
Ioan Pop can be contacted at: ipop@math.ubbcluj.ro